7 Electron Transport and Redox Reactions in Solid-State Molecular Electronic Devices

Richard McCreery

CONTENTS

7.1 INTRODUCTION AND SCOPE

A core concept in electrochemistry is activated electron transfer (ET) between an electrode, usually a conducting solid, and a redox system in the nearby solution. The vast literature on ET kinetics describes the importance of ET to chemical and biological processes, and the underlying phenomenon of coupling a chemical reaction to the flow of current is the basis of >$300 billion of annual gross national product. Chapter 1 in this volume describes ET in nanoscale systems, mainly at an interface between an electrode and an electrolyte solution. A widely studied example of ET kinetics of relevance to the current chapter deals with ET occurring through a self-assembled monolayer (SAM) to a redox molecule (e.g., ferrocene) bonded to the SAM at the solution interface,[1–3] as shown in Figure 7.1a. Such experiments stimulated a large research effort to understand the relationship between ET from a solid to a redox system through a nonredox active SAM and the thoroughly investigated dependence of ET within molecules, such as occur in biological metabolism and photosynthesis. An important conclusion about ET at electrodes as well as between two molecules in solution is the fact that the electrode and redox center (or the two redox centers in solution) need not be in direct contact to transfer electrons. It is possible, and quite common, for electrons to transfer through a SAM or intervening spacer (even a vacuum) by quantum mechanical tunneling, as described in Chapters 1 and 6 and in Section 7.3. For ET at both electrodes in solution and between redox centers within molecules, the ET rate depends on the driving force in terms of free energy and on the composition of the intervening solution or molecular structure. In addition to tunneling, ET in such systems may occur by other mechanisms, such as redox exchange, superexchange, and a sequence of ETs between distinct redox centers.[4]

The current chapter deals with ET in solid-state devices, which lack a solution but may involve electron transport, activated redox reactions, and/or ion motion. Extensive past investigations of transport in organic semiconductors, conducting polymers, and redox polymers provide important

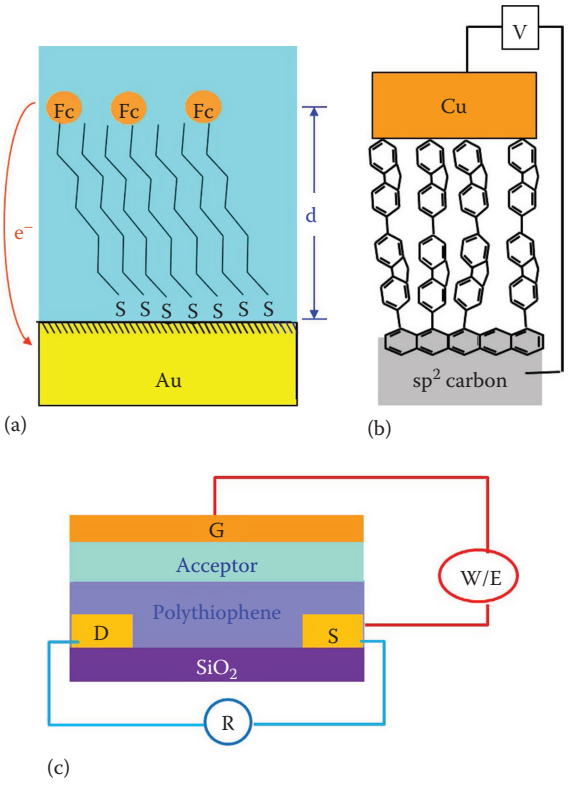

FIGURE 7.1 (a) Schematic of ET between ferrocene (Fc) bonded to Au and a SAM. (b) Two-terminal MJ with a conducting carbon substrate and Cu top contact. (c) Three-terminal molecular memory device with *read* (R) and *W/E* circuits shown.

precedents, in that they all involve electron transport across organic (usually) materials over distances of a few nanometer up to several micrometer. *Organic electronics* is focused mainly on organic films capable of electron transport, with commercial applications in organic light-emitting diodes (OLEDs) and organic field-effect transistors (OFETs). An active area of electrochemistry of the 1980s and 1990s considered ET through polymers such as poly(vinylferrocene) by a series of redox exchange reactions between ferrocene centers in the polymer.[5–8] Such experiments involved variants of the *molecular junction (MJ)* shown in Figure 7.1b, consisting of an organic film between two conducting contacts, with little or no solvent present. ET through a 100–1000 nm thick molecular layer was measured as a current between the two contacts and in some cases was accompanied by ion motion. Starting in the late 1990s, ET in MJs with thicknesses of <10 nm was investigated, and such studies comprise the rapidly growing area of molecular electronics (ME).[9–15] In many cases, the molecular *layer* is a single molecule suspended between two contacts, with one contact being an STM or AFM probe.[16–18] The important distinction between *organic* and *molecular* electronics is one of scale, with the latter involving transport distances of a few nanometer. As summarized in Table 7.1, the >100 nm transport distance common to organic electronics dictates transport consisting of a series of steps, usually activated redox exchange.

The carrier mobility is governed in part by the reorganization energy of the radical ions required for hopping, and transport generally has a positive temperature dependence. The low mobility common to organic semiconductors compared to silicon has been a serious drawback of organic electronics, as has low stability resulting from carriers consisting of radical ions. Reduction of the transport distance to <10 nm enables other ET mechanisms such as tunneling and may avoid

TABLE 7.1
Comparison of Organic and Molecular Electronics Highlighting Differences in Distance Scale, Mechanism, and Electric Fields across the Molecules

	Transport Distance	Temperature Dependence (σ = Conductivity)	Transport Mechanism	Electric Fields (V cm^{-1})
Organic electronics	0.1–100 μm	$d\sigma/dt > 0$	Redox exchange variable range hopping	10^3–10^4
Molecular electronics	1–10 nm	??	Tunneling, *off resonance injection*, ??	10^6–10^7

formation of reactive intermediates. Furthermore, the electric fields in MJs may be much higher than those in OLEDs and OTFTs, often exceeding 10^6 V cm^{-1}.[13] As noted in Section 7.3, these high fields can have major consequences to the ET mechanism.

In addition to ET across short distances in MJs, this chapter also considers memory devices in which a redox reaction results in a large change in conductance in a device with the geometry shown in Figure 7.1c. Although its arrangement is similar to that of an OFET, its operation is fundamentally different, as described in Section 7.4. Solid-state nonvolatile memory (NVM) has enabled portable electronics, with broad applications in cell phones and portable music players, and replaced disk drives in laptop computers.[19,20] The large demand for NVM has driven an extensive research effort on alternatives to existing dynamic random access memory (DRAM) and *flash* memory based on the silicon floating gate structure. *Flash* memory is a successful example of NVM based on the silicon floating gate field-effect transistor (FET), widely used in portable consumer electronics such as smartphones and USB drives.[21] Flash memory has retention times exceeding 10 years; can be very dense, for example, >10 GB cm^{-2}; and is inexpensive enough for widespread use. Flash uses a relatively high-voltage pulse (~10 V) to inject electrons into a floating gate of silicon on silicon oxide insulator. The resulting field from the trapped charge then modulates the conductance of a FET, and the low and high conductance states can be read nondestructively to provide a *bit* of information storage. However, the high-voltage requirement leads to relatively high energy requirements for write/erase (W/E) operations, and fatigue of the SiOx *gate oxide* leads to limited cycle life.[21] In addition, flash is subject to cross talk between adjacent cells, which ultimately limits its information density. Furthermore, flash is much slower than DRAM based on charge storage on a capacitor, and its limited cycle life prevents many applications where long retention is desirable.

Many *alternative* NVM devices involve redox processes of both organic[20,22,23] and inorganic[24–27] materials, although none of these have penetrated the commercial market. An example of redox-based memory where commercialization was attempted is a dynamic memory element in which charge is stored in a porphyrin redox center instead of a capacitor. The porphyrin device had potentially higher density, lower cost, and longer retention time than currently very common DRAM.[23,28] A single bit of the porphyrin-based memory is essentially a very small battery having two redox systems and mobile ions, with significantly higher charge density than possible with a capacitor of similar size. An important but fairly obvious aspect of redox-based memory devices is that redox reactions are difficult or impossible in silicon, and the active memory element nearly always involves addition of a metal, metal oxide, or organic redox element.

An additional important feature of more recently developed memory devices, including *flash*, is their readout based on resistance[29–33] rather than electronic charge or magnetism. The charge-storage mechanism used in DRAM limits retention time due to leakage from a very small capacitor, limits density to a minimum readable charge on the capacitor, and also increases cost due to the need for a high aspect ratio *trench* capacitor.[23] The long retention, nondestructive readout, and high bit density of *flash* are the main reasons for its widespread use, but the cycle life of ~10^4 W/E cycles

constrains its use to applications with relatively low duty cycle. Some of the newer NVM alternatives based on redox processes, including that shown in Figure 7.1c, also involve resistance readout to exploit its advantages, but seek to increase lifetime and reduce energy consumption. As an indication of the breadth of the research effort into alternative NVM, a SciFinder search yielded >14,000 citations for either of the terms *resistance memory* and *conductance switching*. There is a wide range of mechanisms for achieving a persistent change in conductance, which can then be read by an electronic circuit. However, there is also a significant uncertainty about the mechanism operative in particular devices, with the result that improving performance is not straightforward.[22,24] For the case of redox-based memory devices, electrochemical concepts and techniques should be invaluable for understanding and improving performance.

In the context of nanoelectrochemistry, this chapter describes the relationship between some familiar electrochemical concepts and solid-state devices of potential interest in microelectronics. Specifically, what charge transport mechanisms are operative when the transport distance decreases below the ~100 nm typical of organic electronic devices and redox polymers? Do the electrified interfaces or high electric fields in molecular layers with 1–20 nm thicknesses result in redox events? Can redox-based resistance memory exhibit improved performance over commonly used commercial devices? What electrochemical processes control such memory devices and what are the fundamental limits to performance? Section 7.2 describes fabrication of MJs of both the two-terminal (Figure 7.1b) and three-terminal (Figure 7.1c) configurations. Section 7.3 describes electron transport across two-terminal devices with thickness in the range of 4–22 nm, with emphasis on transport mechanism and electronic behavior. Section 7.4 describes resistance memory devices based on redox reactions in conducting polymers and their potential applications as alternative NVM. Finally, Section 7.5 considers future prospects for nanometric molecular electronic devices, both in fundamental science and commercial applications.

7.2 FABRICATION OF MOLECULAR ELECTRONIC DEVICES

As already noted in Figure 7.1, an MJ is derived from the modified electrodes in common use in solution phase electrochemistry. Some additional comments are appropriate when considering modified surfaces in the context of possible microelectronic applications. Obviously, many existing components of today's microelectronics are also two- or three-terminal, and their functions depend strongly on which configuration is employed. The two-terminal geometry shown in Figure 7.1b is equivalent to a modified electrode with the solution replaced by a conductor and is intended to lack ions and solvent and usually mass transport. As will be discussed in Section 7.4, the three-terminal geometry of Figure 7.1c provides a *control* electrode (denoted as "G" in the figure) and can also have some of the properties of an electrochemical cell. There have been many variations on fabrication of both two- and three-terminal molecular devices, usually classified by the type of surface bonding between the molecular component and the conducting substrate.[13–15,34–36] These many variations will not be reviewed here, but some special concerns about the structures shown in Figure 7.1 will be considered, in order to illustrate the transition from modified electrodes (Figure 7.1a) to molecular electronic devices (Figure 7.1b and c), namely, substrate patterning and flatness, molecular layer bonding and formation, and top contact deposition.

7.2.1 Fabrication of Two-Terminal Molecular Junctions

Most applications of ME will likely involve the wafer-scale, massively parallel processing currently employed in the microelectronics industry. Therefore, MJ fabrication must be compatible with photolithography and reasonable temperature excursions during processing and operation. In addition, the substrate must be very flat, so that its root-mean-square (RMS) roughness is significantly less than the thickness of the molecular layer. Our approach to addressing these issues is the use of the unique properties of carbon–carbon bonding possible by diazonium reduction on sp^2 carbon

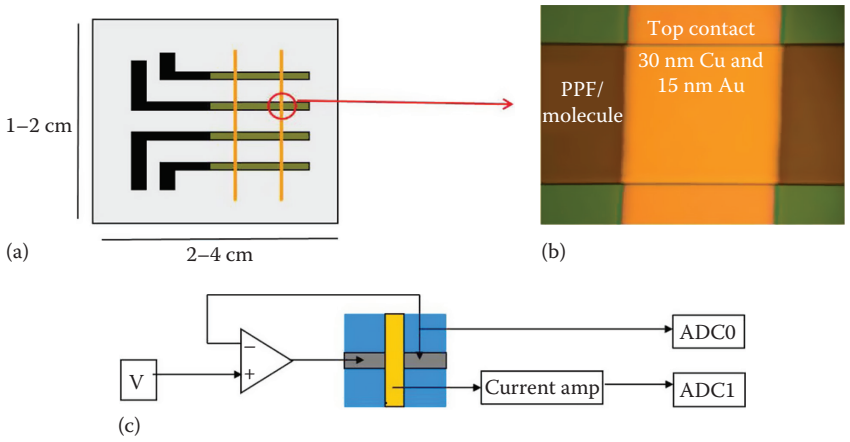

FIGURE 7.2 (a) Substrate pattern for two-terminal MJs, starting with four *stripes* of PPF on an insulating Si/SiO_2 chip and then a magnified image of the finished MJ (b). (c) The three-electrode schematic that corrects for ohmic potential error in the PPF.

surfaces.[14,37,38] Pyrolyzed photoresist film (PPF) is a form of glassy carbon made by pyrolysis of commercial photoresist resins (mainly *novolac*), which can be patterned by conventional photolithography.[39–42] Heat treatment in 5% H_2 in N_2 (i.e., *forming gas*) provides a reducing atmosphere that produces a very flat (<0.5 nm RMS by AFM) sp^2 hybridized carbon surface in the same pattern as the original photoresist.[40] PPF has electronic, electrochemical, and structural properties similar to glassy carbon, and its surface presumably consists of a random array of basal and edge regions of the sp^2 carbon. Figure 7.2a shows the pattern used for many *laboratory* devices, in which a given sample has 4–12 MJs, consisting of a 200–500 μm wide PPF strip with a 100–250 μm wide *top contact*, in this case Cu and Au.

An image of an MJ is shown in Figure 7.2b, and contact is made with probes (usually tungsten) positioned on the MJ as shown in Figure 7.2c. Notice that the three-wire measurement geometry shown in Figure 7.2c is analogous to that used in electrochemistry and provides compensation of the ohmic potential drop in the PPF lead.[43] Microfabrication of MJs at the level of a 100 mm diameter wafer is shown in Figure 7.3, starting with a mask (panel a) followed by pyrolysis to generate a wafer of PPF patterns (panel b), which are then diced into individual samples and modified further (panels c and d).[44]

Diazonium reduction to form C–C bonds on sp^2 surfaces has been studied extensively[45–50] and is well suited to MJ fabrication for several reasons. First, the C–C bond is thermally stable, at least up to >500°C, and is formed mainly at the edges of graphitic sheets on the PPF surface.[51,52] Second, surface modification is mediated by a phenyl radical, which aggressively *patches* pinholes on the PPF surface, leading to high coverage. Although the radical mechanism can also produce multilayers, the layer is covalent and conjugated, and its thickness can be verified by AFM *scratching*.[53] Third, the conjugated phenyl–phenyl bond between the molecular layer and the PPF may have special electronic consequences, as it represents an example of strong electronic coupling, as discussed in Section 7.3. The molecular layer is usually deposited electrochemically, by immersing the PPF *stripes* shown in Figure 7.2a or the microfabricated chip of 7.3 in an electrolyte solution containing the appropriate diazonium reagent. Repeated negative voltammetric scans are then used to build up a molecular layer with thickness in the range of 2–25 nm. The RMS roughness of the modified layer matches that of the substrate (<0.5 nm) for molecular layers up to ~6 nm and increases slightly to <1 nm for 22 nm films.[54] An example of the statistical analysis currently used to determine layer thickness is shown in Figure 7.4, with the 10.3 ± 0.9 nm result reflecting the combined (quadrature) standard deviation of both the PPF substrate and the molecular layer,

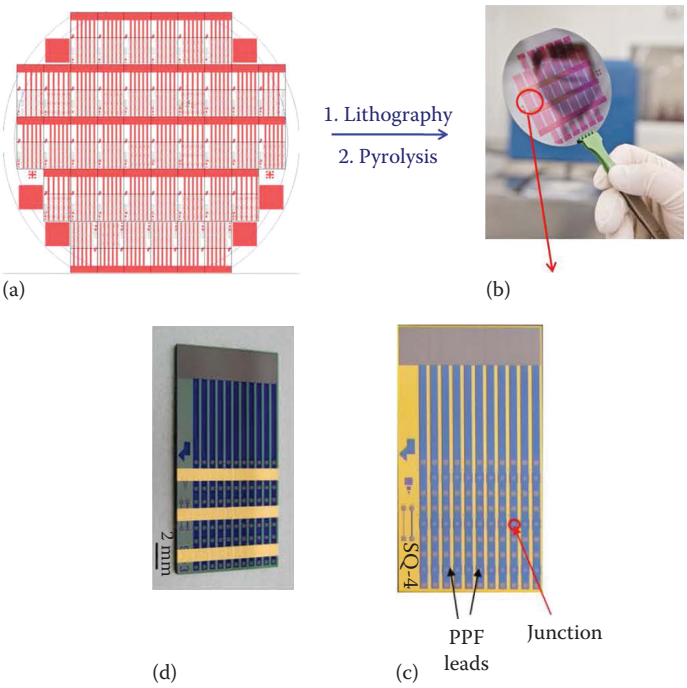

FIGURE 7.3 Photolithography mask (a) and photograph (b) for a PPF pattern on a 100 mm diameter wafer. Pattern includes 40 sample substrates (c) with 32 junctions each, and top contact is applied through a shadow mask to yield finished devices (d).

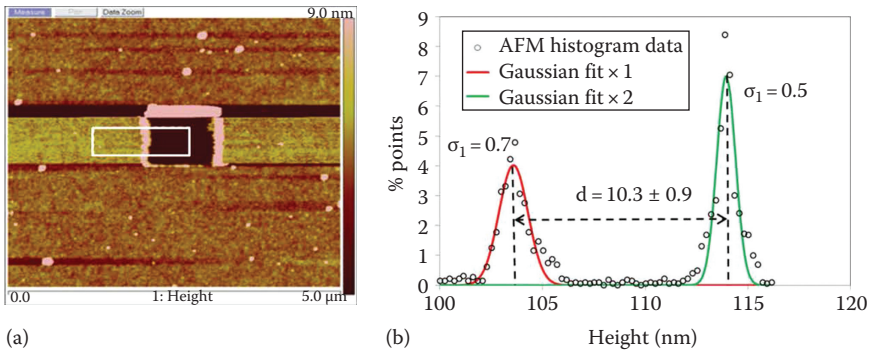

FIGURE 7.4 (a) A modified PPF surface showing a *scratch* made with contact mode AFM with sufficient force to remove the molecular layer. (b) Statistical analysis of the heights determined with tapping mode in the area of the white rectangle. (Used from supporting information of Yan, H. et al., *Proc. Nat. Acad. Sci. U. S. A.*, 110, 5326, 2013. With permission.)

determined at many positions inside and outside an AFM scratch made with the contact mode but analyzed with the *tapping* mode.[54]

In most cases, the thickness determination is performed directly on the sample studied electronically, on the exposed PPF/molecule region adjacent to one of the junctions.

Application of a top contact to complete the MJ has been a very active and often controversial topic, with no consensus emerging yet regarding the best method. The main concern is that common methods based on metal sputtering or vapor deposition can damage and/or penetrate the molecular

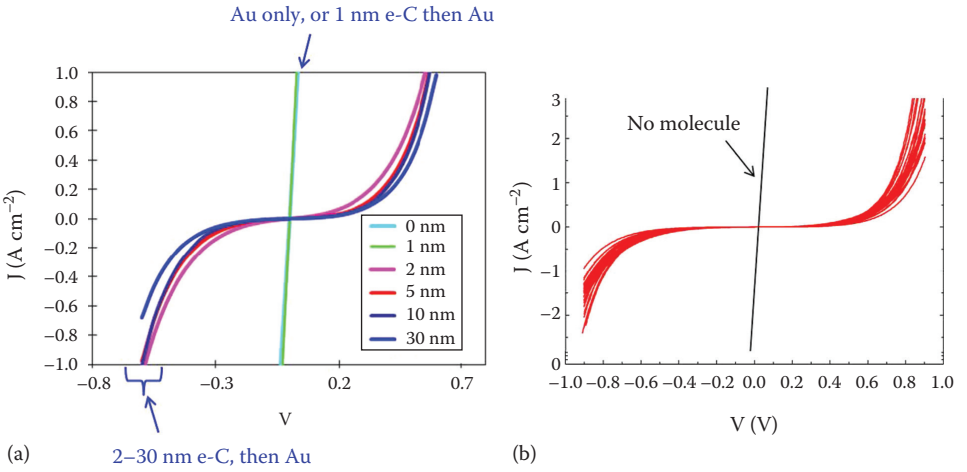

FIGURE 7.5 (a) JV response for MJs made from a 4.1 nm thick layer of NAB on PPF after deposition of various top contacts. The vertical line results from direct deposition of 15 nm of Au on the molecular layer and from deposition of 1 nm of e-C followed by 15 nm of Au. The remaining curves result from deposition of 15 nm of Au on top of the indicated thicknesses of e-C. (b) Overlay of JV curves from 32 NAB junctions on four separate *chips* (red curves) compared to one with the molecule absent. (Used from Yan, H. et al., *J. Am. Chem. Soc*., 133, 19168, 2011. With permission.)

layer, often with the formation of *shorts*, that is, direct electrical contact between the substrate and top electrodes.[55–57] We reviewed these methods[14] and their associated pitfalls, including the importance of structural characterization of completed MJs with optical spectroscopy.[43,58–63] The high coverage and thermal stability of diazonium-derived PPF/molecule layers enable them to tolerate electron beam deposition of Cu, Ag, and Au with minimal effects on the Raman spectrum of the molecular layer. However, deposition of Ti or Pt on the same substrates results in significant changes to the Raman spectrum as well as *shorts*, indicating serious alteration of molecular layer structure.[58] Although Au does not change the Raman spectrum of the molecular layer, it does penetrate the film and results in a short circuit, as shown in Figure 7.5a.

Similar problems with Au deposition on SAMs and Langmuir–Blodgett films have been reported extensively, as has layer damage by Ti.[55–57,65] An alternative *cold* deposition method based on diffusion of metal atoms to contact the molecular layer yields very similar current-voltage response for PPF/molecule/Au MJs, indicating that direct metal deposition does not alter electronic behavior.[66,67] Microscopy images of the MJs depicted in Figure 7.4d at progressively higher magnification are shown in Figure 7.6, starting with a close-up of the junction region in panel a.

A recent alternative to direct metal deposition uses electron beam–deposited carbon (e-C) as the initial top contact, followed by a layer of 15 nm of Au to permit electrical contact.[64] Figure 7.5a shows that a 2 nm thick layer of e-C prevents penetration of subsequently deposited Au, and the final MJ shows response comparable to a similar junction with a Cu/Au top contact.

Although e-C has a higher resistivity than PPF, its thickness may be increased to 30 nm without significant effects on the observed current density. Raman spectra before and after deposition of e-C and Au showed no change in peak positions or relative intensities of the bands of nitroazobenzene (NAB), implying minimal changes to the molecular layer structure. Reproducibility of devices made with e-C (10 nm) and Au (15 nm) top contacts is shown in Figure 7.5b for 32 MJs from four separate samples with eight junctions on each. The 100% yield and rsd of 10%–20% for the current density indicate reliable fabrication and good consistency for finished devices. The e-C/Au top contact also permits a higher range of applied bias and fabrication of thicker MJs, up to at least 22 nm.[54,64]

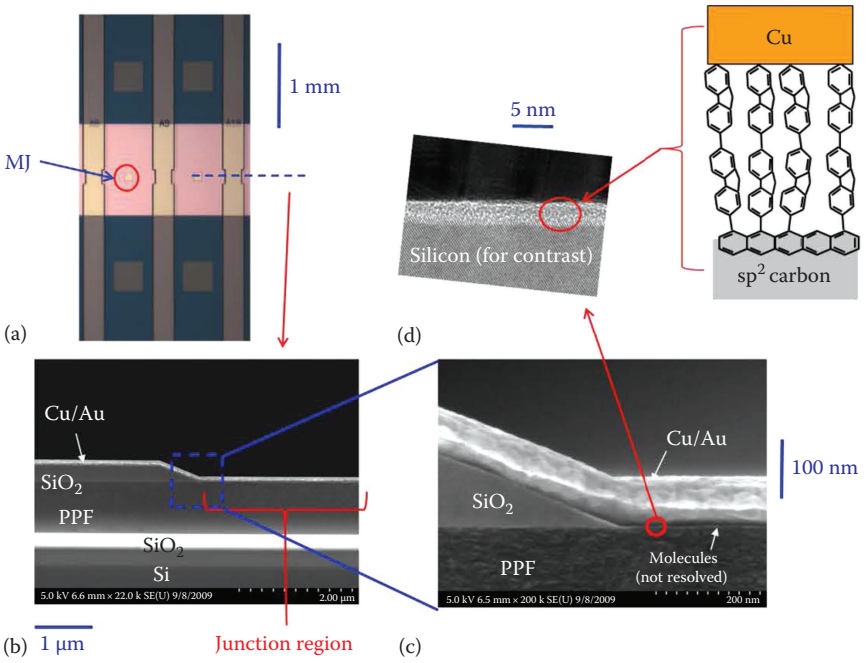

FIGURE 7.6 Micrographs of microfabricated MJs at progressively higher magnifications: (a) Photomicrograph of two junctions and their contact pads. (b) SEM cross section of a junction cleaved at the dotted line in panel A. (c) Magnified SEM of one edge of the MJ showing the metal top contact layer. (d) TEM of molecular layer between silicon and copper, with silicon replacing PPF to provide contrast. (Images a, b, and c used from Ru, J. et al., *ACS Appl. Mater. Inter.*, 2, 3693, 2010. With permission.)

7.2.2 Fabrication of Three-Terminal Molecular Memory Devices

Since the early experimental work on ME in the late 1990s, memory devices have been prominent, due to the large commercial incentive to make solid-state memory that is more dense and faster or requires less power than current technology. Many of these devices were two-terminal, often a *crossbar* arrangement, and were in principle scalable to very small device size, with possibly even a single molecule representing one *bit*.[9,60] As noted in Section 7.1, a wide range of devices has been reported for both organic and inorganic memory devices with both two- and three-terminal geometry having mechanisms involving distinct physical phenomena. We investigated a two-terminal device based on conductance changes in a layer of TiO_2 adjacent to a molecular layer of NAB or polypyrrole (PPy). Although these devices showed initial promise, they proved to be unreliable due in part to the requirement that the two contacts must perform both W/E and read (R) operations. As described in Section 7.4, we then adopted the configuration of Figure 7.1c, consisting of a conducting polymer (poly(3,3′-didodecylquaterthiophene) [PQT] in the case shown) and a third electrode (labeled "G" by analogy to the gate of a FET). Note that the W/E and R circuits are now separated, so these operations can be controlled independently. In addition, the *read* process is nondestructive and in principle very fast. We use the "S," "D," "G" labeling from FET technology due to their familiarity, but the operation of the memory device differs fundamentally from that of a FET.

Fabrication of three-terminal memory devices is derived in part from the lithography and spin coating methods common to the very active OFET literature, but with some special requirements dictated by the need for mobile ions and redox-based conductance changes. A research test substrate for a one-bit memory device is shown in Figure 7.7a, with a 20 µm gap between the S and D electrodes. The pattern on the substrate includes S and D electrodes, onto which the polymer layers

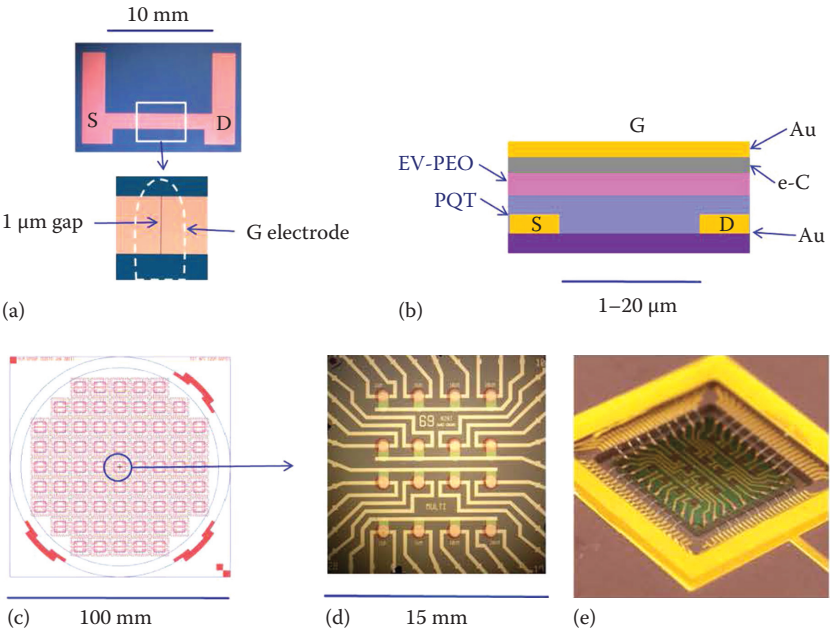

FIGURE 7.7 (a) Top view of three-terminal substrate showing S and D electrodes (upper) and the location of the G electrode (lower). (b) Side view schematic of redox-gated memory device. (c) Mask for microfabricated devices shown enlarged in panel (d) and wire bonded in a package in E.

are spin coated. Regioregular PQT is a polythiophene derivative made by Xerox Research Centre of Canada for application in OFETs and printable electronics,[68–70] and it is first applied to the SD substrate by spin coating. The EV–PEO layer is then either drop cast or spin coated on top of the PQT layer, to build up the structure shown from a side view in Figure 7.7b.

Finally, an e-C (15 nm) and Au (15 nm) are applied by e-beam deposition through a shadow mask to complete the device. Most of our research on redox-gated memory devices to date was done with the *laboratory* substrate of Figure 7.7a,[34,71–73] but the entire process can be adapted to parallel fabrication using the substrate shown in Figure 7.7c through 7.7e. Each unit in a pattern on a 100 mm wafer (8C) has 16 test cells (8D) onto which polymers can be applied. The test chip can then be mounted in commercial packaging by wire bonding (Figure 7.7e) to permit environmental and lifetime testing.

7.3 ELECTRON TRANSPORT ACROSS NANOMETER-SCALE MOLECULAR LAYERS

As noted in Section 7.1, electron transport in MJs has important similarities to ET through monolayers on modified electrodes. Transport by tunneling in both cases is shown in Figure 7.8 for a conducting carbon electrode. The density of electronic states in a conductor is high, and the distribution of electrons in these states is dictated by the Fermi function, which defines the Fermi level as the energy level that is half filled with electrons. The wave nature of electrons dictates that there is finite electron density outside the carbon electrode that extends into space or into a solution with an exponentially decreasing *tail*, as shown in Figure 7.8a.

Stated differently, an electron has finite probability of being located *outside* the electrode itself, with the probability dictated by both distance and the nature of the material adjacent to the electrode. A reducible compound such as anthracene (AN) in solution approaching the electrode surface will

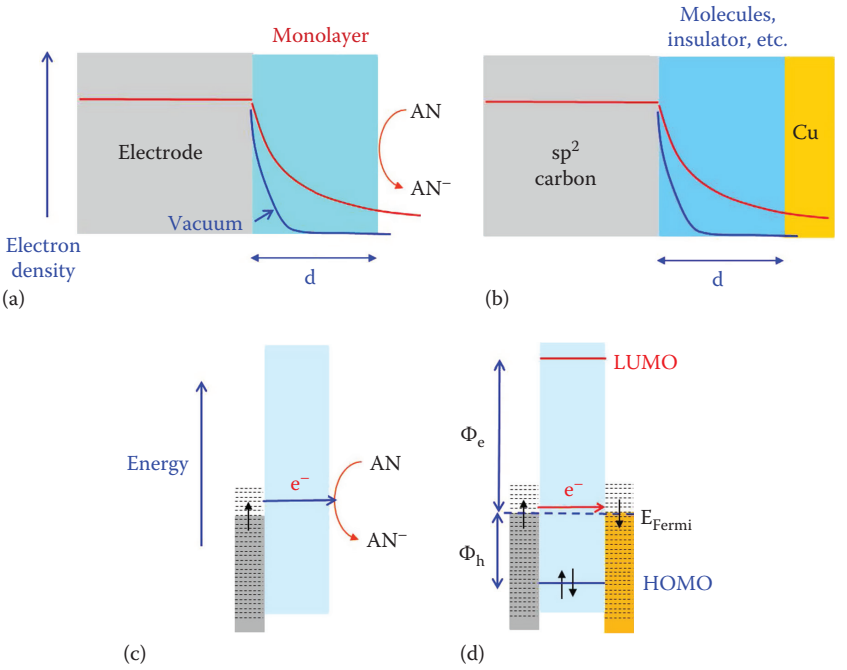

FIGURE 7.8 (a) Schematic of electron density vs. distance for a modified electrode reducing a redox system in solution. (b) Same schematic for a MJ with Cu replacing the solution. (c) Energy levels for the process of panel (a), with shaded area representing filled states in the electrode and an electron tunneling through the molecular layer. (d) Energy levels for an MJ, with HOMO and LUMO representing the highest occupied and lowest unoccupied molecular orbitals of the molecular layer. Φ_e and Φ_h indicate the electron and hole tunneling barriers, respectively.

first encounter the *tail* of electrons, and an electron may transfer to the electrode even though the AN is not actually in direct contact with the electrode surface. The rate of ET through the monolayer is strongly dependent on the nature of the monolayer, as well as the usual parameters related to reorganization energy, transfer coefficient, etc.[1–4,74] A wealth of experimental and theoretical results supports an exponential dependence of ET on the thickness of the monolayer (d), according to Equation 7.1:

$$k°(obs) = k°(d=0)\exp(-\beta d) \tag{7.1}$$

where

$k°(obs)$ is the observed heterogeneous ET rate constant
$k°\ (d=0)$ is the rate constant with the monolayer absent
β is the attenuation parameter, with units of $Å^{-1}$ or nm^{-1} (nm^{-1} will be used here for consistency with the figures)

Therefore, a β equal to 1.0 nm^{-1} indicates that the ET rate decreases by 1/e (or 63%) for every nanometer of monolayer thickness. Equation 7.1 has been applied to a variety of ET reactions in electrochemistry as well as intramolecular and intermolecular ET occurring in homogeneous solutions. This literature is extensive, but relevant benchmark β values include 8–9 nm^{-1} for ET through alkane chains; 3–5 nm^{-1} for conjugated, aromatic molecules; and as low as 1–2 nm^{-1} for the conjugated backbone of polyolefins.[14] β for a vacuum depends on the electrode work function, but is high, typically ~25 nm^{-1}. So although an electron can tunnel through a vacuum, the range of distances is very short, with the probability of ET decreasing to less than 1% with a vacuum gap less than

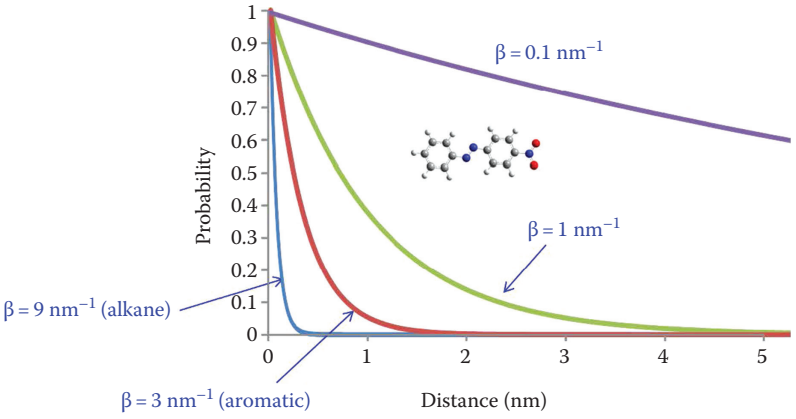

FIGURE 7.9 Prediction of probability of finding an electron at some distance from an electrode as a simple function of exp(–βd) for the indicated values of β. A 1.3 nm NAB molecule is shown for scale.

2 Å thick. Figure 7.9 shows the probability distribution for electrons with distance from a surface for various β values, along with a typical molecule (NAB) to indicate the scale.

An MJ can be considered a modified electrode with the solution replaced by a conductor, as shown in Figure 7.8b. This case is the classical metal/insulator/metal (MIM) device that was first treated theoretically in the 1960s[75–77] to describe tunneling in metal or silicon oxides. A redox reaction need not be involved, and the observed current follows the empirical relationship of Equation 7.2. The absence of a redox reaction

$$J\ (A\ cm^{-2}) = B(A\ cm^{-2})\ \exp\ (-\beta d) \tag{7.2}$$

simplifies the process significantly, since there is no mass transport, reorganization energy, or reaction kinetics. The common depiction of energy levels in the MIM system is shown in Figure 7.8d for a vacuum gap and an MJ. The levels in the conductors are shown as a continuum, with a constant density of electronic states usually assumed for simplicity. The shaded areas represent filled electronic states, up to a Fermi level that may differ for various conductors. For a vacuum gap, the tunneling barrier equals the work function of the contact material, since removal of an electron from the contact produces a free electron in vacuum. Adding a molecular layer between the two contacts to make the MJ shown in Figure 7.10d introduces HOMO and LUMO (highest occupied and lowest unoccupied molecular orbitals) levels into the *gap*, and these are generally assumed to straddle the contact Fermi levels, as shown. If the HOMO occurred at a higher energy than the Fermi level (or the LUMO at lower energy), there would be spontaneous ET between the molecule and the contact and the energies of both phases would change, leading to an entirely different situation. Note that the simple picture of Figure 7.10d ignores charge transfer and energy level realignment when the molecule and contacts are brought together, an assumption often referred to as the *Mott–Schottky limit* in the semiconductor literature.[78–80] As described later, this assumption can often be violated, with significant consequences to device behavior.

The tunneling barriers predicted in the Mott–Schottky limit are shown in Figure 7.8d, for both electron and hole tunneling. For the case of equal Fermi levels of the two contacts, the electron tunneling barrier Φ_e equals $E_{LUMO} - E_F$, with both referenced to the vacuum level. This barrier may be significantly lower than the contact work function; hence, tunneling through a molecular layer may be much more efficient than through a vacuum. *Hole tunneling* is less intuitive but occurs when $\Phi_h = E_F - E_{HOMO}$ is smaller than Φ_e. The only particle actually moving is an electron, of course, but *hole tunneling* may be viewed as starting with transport of an electron in the HOMO level rather than the contact and may become quite efficient if the HOMO level is close to E_F.

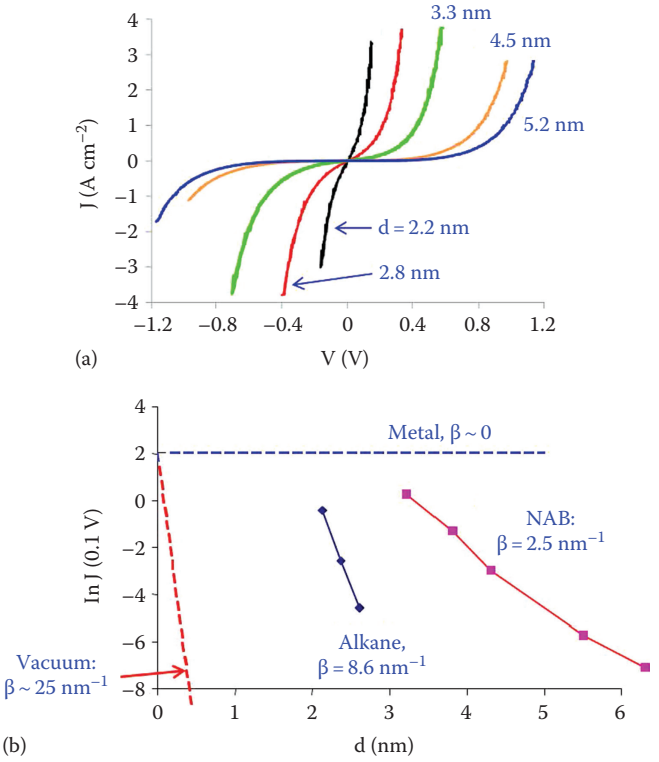

FIGURE 7.10 (a) JV responses of PPF/NAB/Cu MJs with varying NAB layer thickness between 2.2 and 5.2 nm. (b) Plot of ln J(0.1 V) vs. layer thickness for experimental results for alkane and NAB devices and predicted lines for a metal and vacuum. (Alkane data from Bonifas, A.P. and McCreery, R.L., *Nat. Nanotechnol.*, 5, 612, 2010.)

Extensive theoretical treatments of tunneling in MIM devices are based either on the *Simmons* model, which assumes a continuous *insulator* layer with an average barrier height,[75–77,81] or the *Landauer* approach, which is based on predicting the probability of tunneling through a single molecule between the contacts.[12,82,83] These models will not be discussed here in any detail, but they both are consistent with the observed thickness dependence, that is, Equation 7.2. Although both approaches lead to similar predictions of the tunneling rate based on molecule and contact energy levels, the Simmons approach is more readily applied to junctions containing a large number of molecules, while the Landauer treatment is often used for single-molecule devices.[12]

Many types of MJs have been fabricated in order to determine electron transport mechanisms, and many of those have been analyzed in the context of Equation 7.2, to determine if tunneling is the major contributor to the current. We have reviewed the various paradigms for studying conduction in single molecules and *large area* MJs, including some advantages and problems with each approach.[13–15,38] Chapter 6 in this volume describes many experiments on single molecules, including factors that determine electron transport in single-molecule junctions. The results discussed in the current section are based on carbon/molecule/metal devices described in Section 7.2, which illustrate several important factors affecting device conduction. Figure 7.5a shows the current density vs. voltage (JV) response for PPF/NAB(4.5)/e-C(10)/Au(15) MJs, compared to the same device with the molecular layer absent.[64] As indicated in Figure 7.5b, such MJs are quite reproducible, with JV curves that differ dramatically from that of a direct PPF/e-C/Au *short circuit*. A ln(J) vs. V plot is linear above about 0.3 V, indicating that the current increases exponentially with applied bias[37,64,78] and can exceed 400 A cm^{-2} without degradation.[44] The response is weakly dependent

on temperature, with an apparent Arrhenius barrier of <0.2 meV for the range of 5–250 K and <100 meV for the 260–450 K range.[37] The <100 meV *activation* can be attributed to broadening of the Fermi function in the contact, implying that ET is not dependent on molecular reorganization or nuclear motion over the entire 5–450 K temperature range.[37] The JV response was independent of scan rate between 0.1 and 1000 V s^{-1}, and scans to ±1 A cm^{-2} could be repeated for at least 10^9 cycles without observable changes in response. Similar PPF/NAB/Cu devices were tolerant of processing temperatures up to 350°C, as well as a complete photolithography cycle (spin coating, UV exposure, and developing) performed directly on a finished MJ.[58]

Figure 7.10a shows the dependence of JV response on molecular layer thickness (d) for NAB multilayers in the range of 2.2–5.2 nm, with the thicknesses verified with AFM *scratching*.[53] The strong variation of current density with thickness is not expected if the molecules were behaving like resistors, which should yield a 1/d dependence. Figure 7.10b shows a plot of ln J (0.1 V) vs. d for the curves of Figure 7.10a, demonstrating an exponential dependence of J on thickness, as predicted from Equation 7.2. The attenuation coefficient β is 2.5 nm^{-1} for NAB, corresponding to a decrease of J by a factor of $1/e^{2.5}$ or 0.082 for each nm of molecular layer thickness. Also shown in Figure 7.10b are results for alkane junctions made by bonding alkyl amines to PPF by oxidation, which exhibited a $\beta = 8.8$ nm^{-1}.[66] β for the alkane MJs compares favorably with that noted earlier for ET through molecules in solution, and ET across SAMs on electrodes, implying that similar effects control transport rate. Furthermore, the weak temperature dependence over a 5–450 K range is consistent with a tunneling mechanism, presumably controlled by barriers defined by either the molecular HOMO or LUMO, as depicted in Figure 7.8d. The β observed for NAB is similar to that reported for ET through similar aromatic layers on glassy carbon electrodes in solution[74] and also with the 2–5 nm^{-1} reported for aromatic SAMs[3] and single aromatic molecules in break junctions.[12]

The consistently lower β observed for aromatic compared to aliphatic molecules in MJs implies either a HOMO or LUMO that is closer to the contact Fermi level and also indicates an important variable for using molecular structure to *tune* the electronic properties of the MJ. Analysis of JV curves such as Figure 7.10a with the Simmons equations incorporating effective mass and image charge effects yielded tunneling barriers of 1.07–1.25 eV for NAB in the range of d = 2.8–5.2 nm, implying that the main transport mode is hole tunneling mediated by the HOMO level.[37] An independent determination of energy levels using photocurrents yielded a $E_{HOMO} - E_F$ offset of 1.1 eV for an aromatic MJ and 1.7 eV for an aliphatic MJ,[84] completely consistent with the attenuation plots of Figure 7.10b.

The prospect of controlling junction conductance by changes in molecular structure is quite attractive, since there are many molecules available, and *rational design* of MJs with useful electronic behaviors may be possible. The approach of Figure 7.10 was extended to a series of seven aromatic molecules, chosen to have a range of 2.3 eV for both the LUMO energies and HOMO energies of the free molecules.[78] PPF/molecule/Cu MJs were constructed from the seven molecules with various molecular layer thicknesses, for a total of >400 junctions, and then JV curves were obtained at room temperature. The range of molecular energy levels should have resulted in a similar range of tunneling barriers for either electrons or holes if the free molecule energies did not change significantly upon formation of the MJ. As shown in Figure 7.11, the aromatic junctions differed little from NAB, with an average β value of 2.7 ± 0.6 nm^{-1}. While the difference between the aromatic and aliphatic devices was clearly statistically significant, those for the aromatic junctions were not, counter to the expectation from the free molecule HOMO or LUMO energies.[78]

Not only did the aromatic molecules have similar slopes for the lnJ vs. d plots, their current magnitudes were also similar and statistically indistinguishable. The reason for this similarity was revealed by independent measurements of the work functions and HOMO levels using ultraviolet photoelectron spectroscopy (UPS)[78] and photocurrent measurements.[84] Strong electronic coupling between the PPF substrate and the bonded, aromatic molecule resulted in charge exchange between the PPF and the molecule, leading to a *leveling effect* that resulted in similar tunneling barriers of

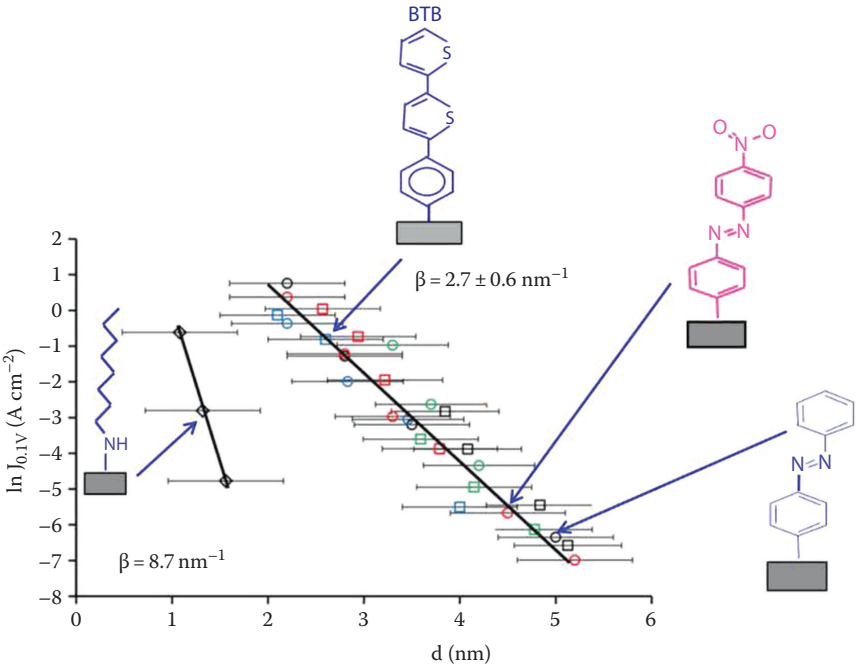

FIGURE 7.11 Attenuation plots from >400 MJs with the indicated molecules plus bromophenyl, ethynyl benzene, anthraquinone, and nitrophenyl molecular layers. (Adapted from Sayed, S.Y. et al., *Proc. Natl. Acad. Sci. U. S. A.*, 109, 11498, 2012. With permission.)

1.3 ± 0.2 eV for all seven aromatic molecules. In effect, the addition of electron donating or withdrawing groups to the aromatic molecule caused shifts in both the apparent PPF work function and the molecular HOMO level, which *compressed* the tunneling barriers expected for the free molecules to a common value of ~1.3 eV, as shown schematically in Figure 7.12. In the semiconductor literature, charge transfer between two materials placed into contact causes similar shifts in energy levels and is known as a violation of the Mott–Schottky assumption that the two phases maintain their *free* energy levels when in contact.

The phenomenon has been discussed extensively for interfaces between metals and organic semiconductors and often has major consequences to the device behavior.[34,85–87] In the case of molecular tunnel junctions such as PPF/molecule/Cu, it results in significantly diminished ability to vary the tunneling barrier by varying substituents on a strongly coupled aromatic molecule. As apparent from the clear difference between aromatic and aliphatic MJs shown in Figure 7.11, the electronic properties of the molecule can still have a major effect on transport, but the electronic properties of the *system*, consisting of both contacts and molecules, must be considered.[78]

The MJs considered thus far were limited to thicknesses below 6 nm, due mainly to experimental limitations on molecular layer growth and top contact deposition. A different MJ structure using e-C as a top contact[64] permitted a wider range of thicknesses (4.5–22 nm) in order to investigate transport mechanisms beyond the tunneling limit of ~5 nm. Figure 7.13a shows JV curves for bis-thienyl benzene (BTB) of the type PPF/BTB/e-C/Au, where e-C represents a 10 nm thick layer of e-C. For d < 5 nm, such junctions are quite similar electronically to the analogous PPF/molecule/Cu devices, but are more stable at higher bias.[64] Note that significant current densities (J >1 A cm^{-2}) are achieved for d = 22 nm, where tunneling should be negligible. Figure 7.14 shows the attenuation plot for V = +1 V and a range of temperatures from 6 to 300 K. For d < 8 nm, the slope of 3.0 nm^{-1} is similar to that observed previously (Figure 7.11) and is independent of temperature. For d >15 nm, β ≈ 0 at 300 K, but the current is temperature dependent with an Arrhenius

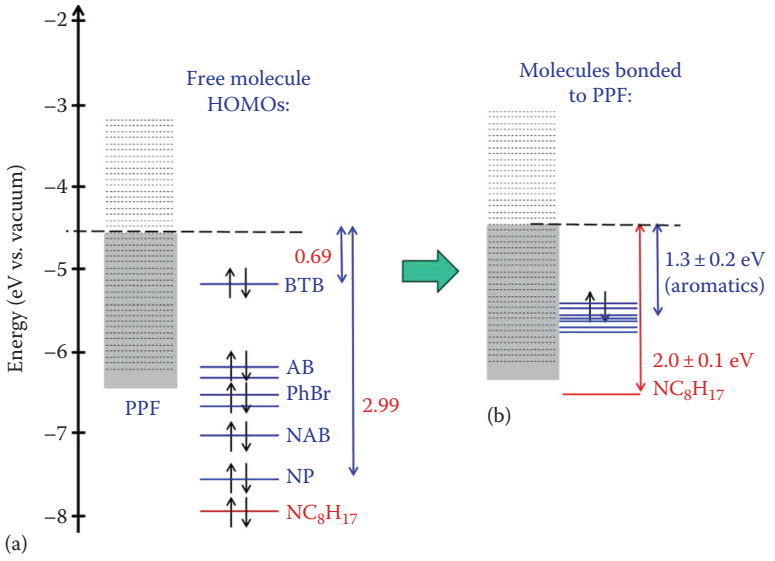

FIGURE 7.12 (a) Energy level diagrams for free molecules calculated with density functional theory [B3LYP 6-31G(d)] on the same scale as the observed work function for PPF (dashed line), predicting tunneling barriers ranging from ~0.7 to ~3 eV. (b) Observed energy levels based on UPS and transport results demonstrating *compression* of the aromatic barriers to values near 1.3 eV. (From Sayed, S.Y. et al., *Proc. Natl. Acad. Sci. U. S. A.*, 109, 11498, 2012.)

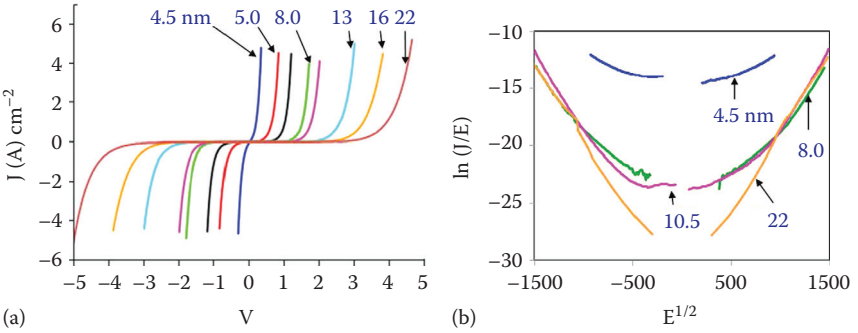

FIGURE 7.13 (a) JV curves for PPF/BTB/e-C/Au MJs with molecular layer thickness from 4.5 to 22 nm. (b) ln(J/E) vs. $E^{1/2}$ plots for selected thickness. Temperature was 300 K in all cases shown. E is the electric field across the molecular layer, assumed to be linear across the device.

slope of 160 meV. For d = 10–16 nm, $\beta = 1$ nm^{-1} and is weakly temperature dependent. Note also that the low-temperature behavior for d = 22 nm is close to the $\beta = 1$ nm^{-1} line observed for all temperatures and d < 16 nm.

A detailed analysis of JV curve shape and temperature dependence resulted in the proposal that three mechanisms were active over the 4.5–22 nm thickness range.[54] For d < 8 nm, transport is dominated by tunneling, and extrapolation of the $\beta = 3$ nm^{-1} line to greater distances indicates that tunneling will decrease below the detection limit at ~12 nm. For d = 22 nm, transport is consistent with thermally activated hopping with an activation energy of 160 meV, with a decrease at low temperature to the same $\beta = 1$ nm^{-1} line observed for d = 12–16 nm. Reported activation energies for transport in bulk polythiophene are in the range of 130–280 meV, so transport in structurally

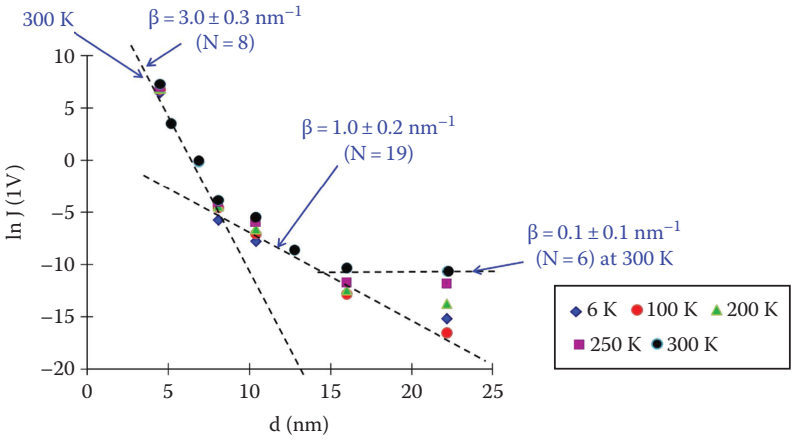

FIGURE 7.14 Attenuation plots for BTB junctions at five temperatures, all obtained with a 1 V bias. Statistics indicate β values for fixed thickness ranges, across several samples and temperatures, as described in Ref. [54].

similar BTB films with d = 22 nm is consistent with redox exchange commonly encountered in organic semiconductors. It is quite likely that the 4.5–22 nm distances shown in Figures 7.14 and 7.15 bridge the *gap* between tunneling transport at short distances and redox exchange operative for *bulk* organic semiconductors.[54]

The nature of transport in the intermediate region with $\beta = 1\ nm^{-1}$ is at least partially revealed by a plot of ln(J/E) vs. $E^{1/2}$ where E is the electric field, assumed to be V/d for a given MJ. Such plots are expected to be linear for Schottky and Poole–Frenkel transport, with the unusual $E^{1/2}$ dependence resulting from the effect of electric field on transport barriers.[88] Figure 7.13b shows this plot for four thicknesses of BTB at room temperature, which leads to two important observations. First, the curves coalesce at high E for d = 8, 10.5, and 22 nm, indicating that transport is *field* dependent over a wide range of thickness, completely inconsistent with tunneling. Second, ln(J/E) vs. $E^{1/2}$ is nearly linear for these thicknesses and high field and is very linear for d = 22 nm and T = 6 K ($R^2 = 0.9899$ over eight orders of magnitude of J/E).[54] These results are consistent with Schottky and Poole–Frenkel transport in one respect; that is, there is a transport barrier that varies with $E^{1/2}$. However, both these mechanisms are based on thermal activation of a carrier over such a barrier, and the $\beta = 1\ nm^{-1}$ mechanism clearly is effective even at 6 K. Therefore, whatever mechanism is proposed for this intermediate region should be *activationless* and effective over a wide range of electric field and temperature. We recently proposed that the intermediate mechanism is based on field ionization of molecular HOMO levels in the molecular layer,[54] conceptually similar to the ionization of electrons in *traps* that is the basis of the Poole–Frenkel mechanism. For d = 10 nm, and a bias of 1 V, the average electric field across the molecule is $10^6\ V\ cm^{-1}$ and much higher than that present in typical organic electronic devices with thicknesses in the 100 nm–10 μm range. Given that the HOMO level of BTB is predicted to be 0.7–1.2 eV below the system Fermi level, Poole–Frenkel theory predicts that ionization of an electron *trapped* in the HOMO may occur when E exceeds $10^6\ V\ cm^{-1}$, which is the point where the curves coalesce in Figure 7.13b.

As outlined in Section 7.5, there is much remaining to be learned about electron transport through nanometric molecular layers, but the current results in addition to those from the literature clearly demonstrate that molecules can act as circuit components and have unusual transport properties.[13] In all of the cases described thus far, transport occurs without conventional redox reactions and is generally weakly activated. We now turn to an approach to molecular memory in which redox reactions are both intentional and essential to the intended application of the molecular electronic device.

7.4 REDOX-MEDIATED SOLID-STATE MOLECULAR MEMORY DEVICES

As noted in Section 7.1, redox reactions have been associated with memory functions in a variety of microelectronic devices, based on both inorganic materials such as TiO_2 and metal filaments[24] and organic materials, notably organic semiconductors.[22] An example of a two-terminal memory device based on resistance switching is shown in Figure 7.15a, consisting of thin layers of PPy and TiO_2 between conducting contacts.

The conductivity of PPy increases by a factor of ~10^8 when it is oxidized by one electron, while that of TiO_2 increases a comparable amount when it is reduced from Ti^{IV} to Ti^{III} oxide.[90] When the PPF electrode shown in Figure 7.15a is biased with the PPF positive, an electron can move in the external circuit from the PPy to the TiO_2, resulting in a major decrease in the resistance between the PPF and Au electrodes. As shown in Figure 7.15c, the resistance may be *read* by standard voltammetry, and the device may be switched repeatedly between the low and high conductance states. Although the electronic characteristics of the PPy/TiO_2 device such as speed, retention, and cycle life were attractive, the mechanism proved complex. Solid-state spectroelectrochemistry of a partially transparent device is shown in Figure 7.15d, demonstrating reversible oxidation of the PPy.[89] However, it was also determined that H_2O was a critical reagent in the process, possibly due to its involvement in redox reactions at one or both electrodes. A detailed examination of TiO_2 revealed a water-mediated reduction and conductance change in TiO_2 alone, without PPy present.[26] These redox events may be involved in any nominally solid-state device containing TiO_2, particularly if they are studied in ambient air. TiO_2 and its bias-induced conductance changes are the basis of significant recent activity on inorganic memory devices dubbed *memristors*, but have not yet been realized commercially.[25,27,91–93]

In addition to the complexity associated with TiO_2, the two-terminal geometry of Figure 7.15a is subject to more fundamental problems with retention and readout. While it has some properties of

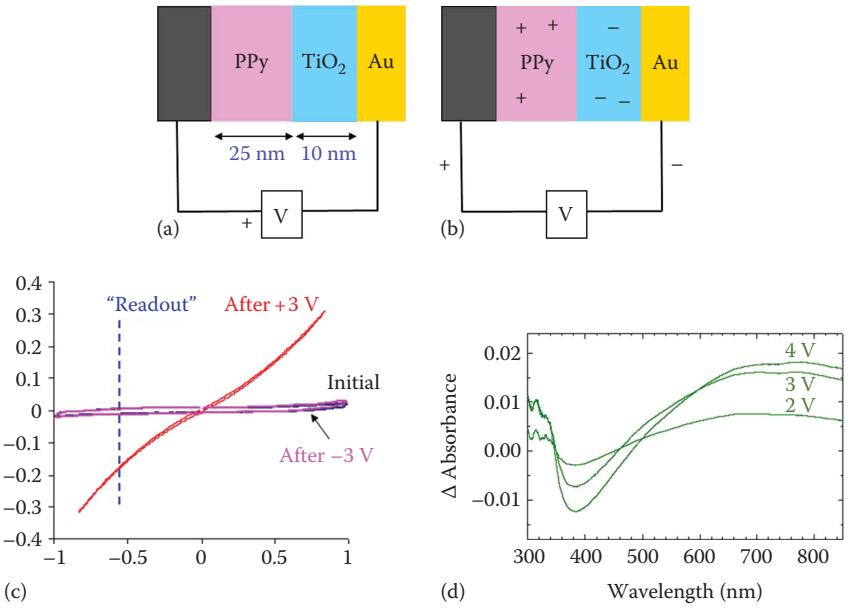

FIGURE 7.15 (a) Two-terminal memory device containing PPy and TiO_2, in its initial low conductance state. (b) The same device after an external voltage causes the conductivity of both layers to increase. (c) IV response of the device following *write* and *erase* pulses. (d) Solid-state spectroelectrochemistry of a PPy/Al_2O_3 device, plotted as the change in absorbance in response to the indicated voltages. (From Bonifas, A.P. and McCreery, R.L., *Anal. Chem.*, 84, 2459, 2012.)

a conventional battery with two redox systems, the redox systems are not physically separated and are subject to recombination reactions at their common interface. Batteries require a separator to prevent such reactions, but introducing a separator into the two-terminal geometry would produce high dc resistance and mask the conductance changes required for memory operation. These recombination reactions will *discharge* the conducting states of the PPy and TiO_2 until the conductance of the device reverts to its initial low value. As long as the two redox systems are in physical contact, retention time will be limited by recombination, and attempts to introduce a separator will unavoidably introduce unacceptably high dc resistance.

In order to avoid both the recombination problem and the complex redox chemistry of TiO_2, we adopted the three-terminal geometry of Figure 7.1c. Initially, the polymer was poly(3-hexyl thiophene) (P3HT), which has a conductivity of $<10^{-7}$ S cm^{-1} in its native form and >1 S cm^{-1} when oxidized by one electron. The configuration of Figure 7.16 was studied with Raman spectroscopy to monitor the oxidation of PQT and correlate it with conductance.[72,73] The conductivity of P3HT is $<10^{-7}$ S cm^{-1} in its native form, which increases to >1 S cm^{-1} when oxidized to its conducting *polaron*.

Although the SiO_2/Pt "G" contact does not include an intentional redox system, it was possible to demonstrate oxidation of the P3HT by changes in its Raman spectrum. Figure 7.16b shows Raman spectra of P3HT in the three-terminal P3HT/SiO_2 device during progressive application of a +4 V bias to the S electrode relative to G. The shift in the prominent Raman band at ~1460 cm^{-1} to lower energy and the appearance of a new band at ~1400 cm^{-1} are the same changes that accompany P3HT oxidation in solution, providing direct evidence for the formation of P3HT polaron.[72] The change in conductance between the S and D electrodes accompanying the spectroscopy experiments is

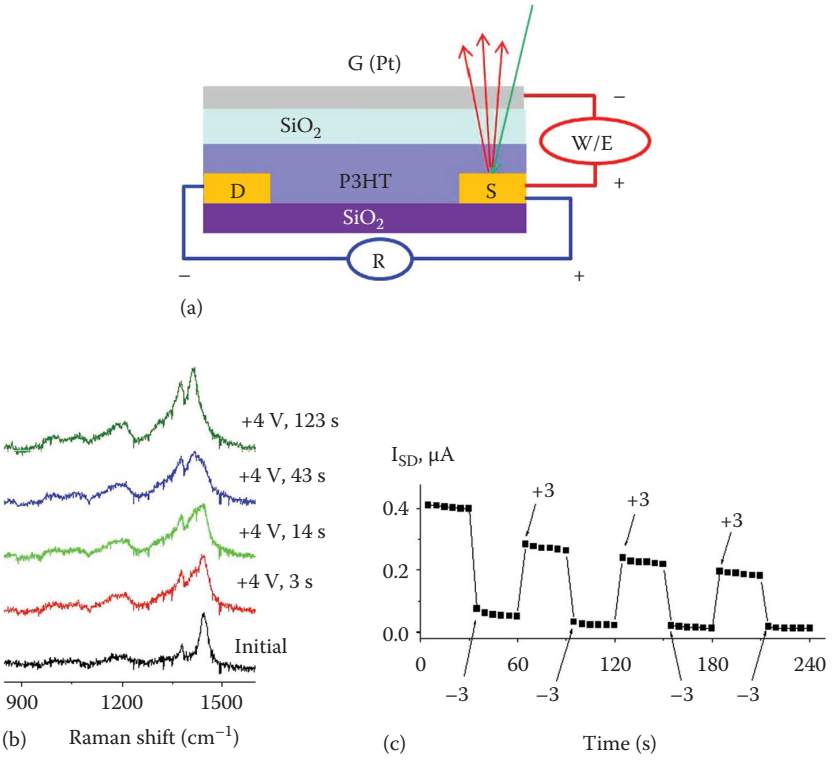

FIGURE 7.16 (a) Schematic of a three-terminal P3HT/SiO_2 memory device showing the incident and Raman scattered light from the source region. (b) Raman spectra of the source region when a +4 V *write* voltage was applied for the times indicated. (c) Repeated changes in SD current in response to *write* (+3 V) and *erase* (–3 V) pulses. (Used from Shoute, L.C.T. et al., *Electrochim. Acta*, 110, 437, 2013. With permission.)

indicated in Figure 7.16c, which is the SD current at a constant applied bias of 0.1 V. Therefore, the P3HT/SiO_2 memory device provides a direct correlation between spectroscopic changes indicating polaron formation and the resulting change in polymer conductivity.

Although the P3HT/SiO_2 device is not suitable for practical application due to its slow W/E times, it does illustrate some merits of the three-terminal geometry and also requirements for useful redox-based memory operation. First, the resistance readout is nondestructive and does not significantly perturb the redox state of the polythiophene. Second, direct spectroscopic monitoring of device operation is possible, which was extended to the spatially resolved experiments described below. Third, the complementary redox reaction accompanying the oxidation of PQT was identified as the reduction of H_2O at the platinum counter electrode (G), and memory operation ceased in a vacuum. While dependence on trace water is undesirable for several reasons, it does illustrate that the redox counterreaction can be spatially separated from the polymer redox events. At least in principle, this situation is required to reduce recombination and extend the retention time. Fourth, the polythiophene active layer avoids the proton transfer reactions of PPy,[89] as well as the complex chemistry of TiO_2. Fifth, the dependence on the presence of water may result from either water's redox reactions or its ability to *solvate* ions and increase ionic mobility, even in a nominally solid-state device. These considerations derived in part from the P3HT/SiO_2 three-terminal example resulted in important design changes intended to improve performance.

It is informative to consider the design introduced in Figure 7.16a as a simple battery, as it illustrates some of the requirements on redox-gated memory devices. Suppose that the two redox systems are a polythiophene on top of the S and D electrodes, and an acceptor layer that contains a viologen derivative, as shown in Figure 7.17a. If the S and D electrodes were one continuous conducting layer, the device is a battery lacking a separator between the anodic and cathodic reactions. It would be possible to charge or discharge the battery, but there would also be a parasitic

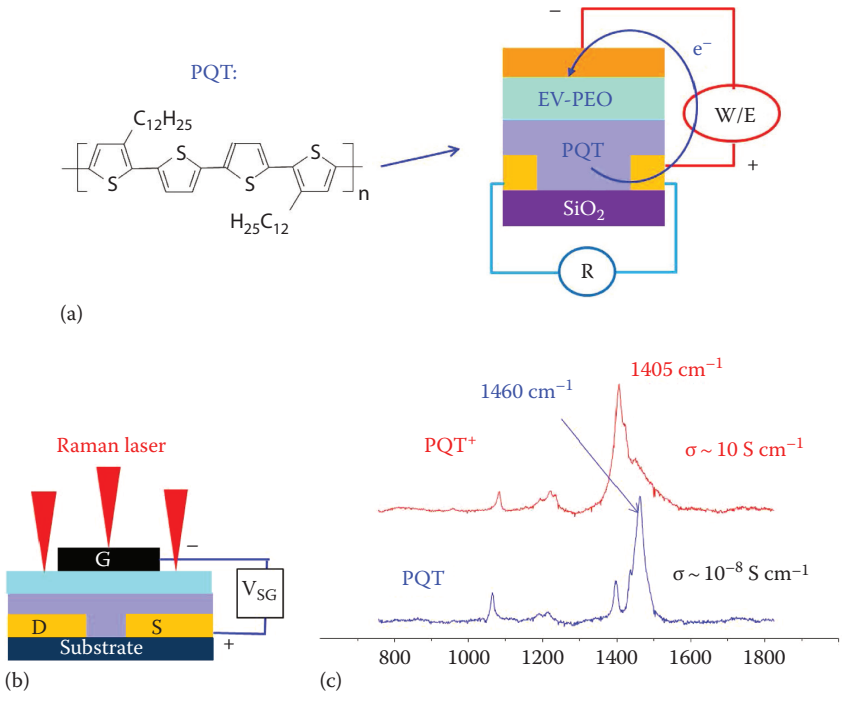

FIGURE 7.17 (a) Three-terminal PQT/viologen memory device, showing EV acceptor in PEO and the PQT structure. (b) Position of incident laser for sampling different regions of the devices. (c) Raman spectra in $CHCl_3$ solution. PEO = polyethylene oxide, EV = ethyl viologen diperchlorate.

recombination reaction at the polythiophene–viologen interface. Separation of the bottom electrode into S and D provides a means to measure the conductance of the polythiophene layer during the charge/discharge process. If a separator were placed between the polythiophene and viologen layers, charging and discharging could still occur, provided the separator permitted ion transport but not electronic conduction. As is well known to electrochemists, a good separator is required in commercial batteries to prevent *chemical* short circuits and is essential to providing long shelf life and long duration of the charged state. By analogy, the three-terminal redox-gated memory configuration is conceptually similar to a conventional battery, with the addition of a second electrode at one contact to permit measurement of conductivity of one of the redox phases. In principle, the speed of such memory devices should depend on the rate of the redox reactions and their associated ion motion, and the retention should depend directly on the properties of the separator.

A design that incorporates all of these design considerations except the separator is shown in Figure 7.17a.[34,71] The polythiophene is regioregular PQT, which was developed for OFETs[68–70] and is chemically and electronically similar to P3HT. Its attractive spin coating properties and higher stability to air oxidation make it amenable to possible commercial applications. The second redox system was ethyl viologen (EV) diperchlorate, an electron acceptor and also a source of mobile ClO_4^- ions. As noted in Section 7.2.2, PQT was spin coated onto a substrate containing the S and D electrodes, and then a mixture of polyethylene oxide (PEO) and $EV(ClO_4)_2$ was drop cast onto the PQT layer to cover the gap between the S and D electrodes. The *write* operation of the intended memory device is indicated by the arrow in Figure 7.18a, consisting of a positive pulse that oxidizes PQT to its conducting polaron and reduces EV^{+2} to EV^{+1}, thus producing a large increase in conductivity in the PQT layer. As is well known, the resulting space charge generated in the PQT and EV layers by the redox reaction must be compensated by ion motion, in this case ClO_4^- ion moving from the EV/PEO layer into the PQT. Formation of a PQT^+ ClO_4^- ion pair in the PQT layer stabilizes the polaron charge to permit a persistent conducting state. As was the case with the $P3HT/SiO_2$ devices, the top contact is thin enough to permit Raman spectroscopy directly in the *gap* region between S and D, as well as other locations on the device, as shown in Figure 7.17b. The Raman spectra of PQT and PQT^+ in chloroform are shown in Figure 7.17d, with the polaron formed by chemical oxidation with $FeCl_3$.

Figure 7.18a shows the solid-state voltammetry of the PQT/EV–PEO memory cell when the voltage between the S and G electrodes is scanned, with the S electrode considered positive by convention. Note that unlike conventional voltammetry, there is no reference electrode, and one

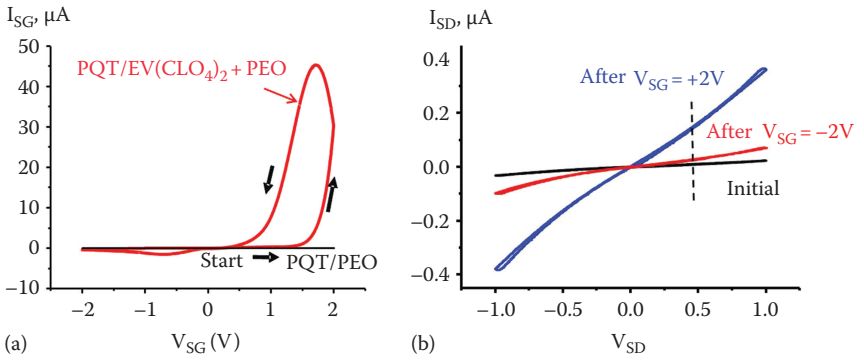

FIGURE 7.18 (a) Voltammetry for three-terminal memory device when V_{SG} is scanned at 50 mV s^{-1} in the presence and absence of EV in the PEO layer, as indicated. (b) SD current when the SD voltage was scanned before and after the indicated *write* (blue) and *erase* (red) voltages were applied. (Used from Kumar, R. et al., *J. Am. Chem. Soc.*, 134, 14869, 2012. With permission.)

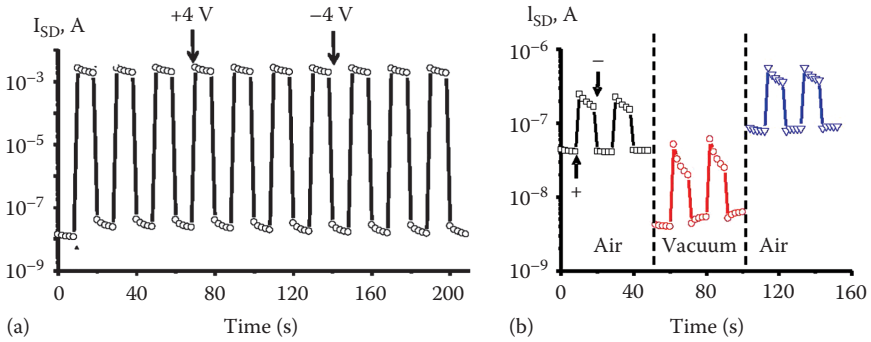

FIGURE 7.19 (a) Ten R/W/E/R cycles for a PQT/EV–PEO memory device in vacuum. Arrows indicate the timing of a typical *write* voltage (+4 V) and *erase* voltage (−4 V) for two cycles. (b) Effect of vacuum treatment and return to air on memory cycles. (Used from Kumar, R. et al., *J. Am. Chem. Soc.*, 134, 14869, 2012. With permission.)

redox system (PQT) is immobile, while the other (EV) is expected to diffuse very slowly in PEO. With EV absent and just the PQT and PEO layers present, the voltammetric current between S and G is very small, as shown by the horizontal black line in Figure 7.18a, indicating that no observable Faradaic reactions occur.

With EV present, I_{SG} increases when the voltage applied between the S and G electrodes exceeds ~1.5 V, with the polarity indicating ET from the S electrode to G in the external SG circuit. The standard potentials (E°) values for PQT/PQT^{+} and $EV^{2+/1+}$ are 0.76 and −0.45 V vs. NHE in solution, so we expect that 1.5 V is sufficient to *charge* the PQT/EV *cell*, thereby generating PQT^{+} and reducing EV^{2+} to EV^{1+}. Since the conductivity of PQT^{+} is much higher than that of the initial PQT, we expect an increase in the SD conductance to accompany the generation of PQT^{+} indicated by the positive I_{SG} current. Figure 7.19b shows the voltammetric response of the SD circuit obtained before and after successive V_{SG} pulses lasting 1 s each. Initially (black curve), the SD current is very small, since the PQT is in its low conductivity state. After $V_{SG}=+2$ V for 1 s, the SD current increases by several orders of magnitude and is approximately linear with voltage, as expected for a partially doped conducting polymer.[71] Reversing the polarity of the V_{SG} pulse to −2 V reduces most of the PQT^{+} back to PQT, and the low conductance state is nearly completely restored.

The voltammetric results of Figure 7.18 illustrate the memory *cycle* depicted in Figure 7.17a, with the SG circuit used for W/E operations and the SD circuit for readout. Consider a constant V_{SD} *readout* voltage of 0.5 V, imposed during various W/E operations and indicated by "R" in Figure 7.17a. The I_{SD} current in response to this fixed V_{SD} would then indicate a "1" or ON state when it exceeds 100 nA in this case or a "0" or OFF state when it is less than 20 nA. The readout process is nondestructive and potentially very fast, since it only requires a transient current measurement. The ON/OFF ratio is often quoted for memory devices and indicates the magnitude of the conductance change between the two states. The $V_{SG}=+2$ V pulse is considered the *write* process, while $V_{SG}=-2$ V is *erase*. In addition to the ON/OFF ratio, important performance indicators for memory devices are the write and erase speed, indicated by the length of the W and E pulses required to yield the desired ON and OFF currents, and *retention* indicated by the stability of the ON and OFF states when the device is left at rest. *Endurance* is a measure of cycle life and indicates the number of W/R/E/R cycles possible before the device fails, with some measure of error rate included in the specification. To provide some context for these parameters, today's DRAM has W/E speeds of 10's of ns and endurance of $>10^{15}$ cycles, but short retention (<100 ms) and destructive readout. *Flash* memory has W speeds of a few μs, ~ms E speeds, and >10 year retention, but limited cycle life (10^{3}–10^{4} W/E cycles). These properties determine the applications

of each memory type in finished products, since *flash* is excellent for long-term data storage, but would rapidly fail if used in processors, while DRAM has excellent speed, but needs to refresh frequently due to short retention.

Repeated W/R/E/R cycles for the PQT/PEO-EV memory cell are shown in Figure 7.19a, for V_{SD} = 0.5 V and W/E pulses of +4/−4 V for 2 s each. Note the logarithmic scale of the I_{SD} readout current and the observed ON/OFF ratio of $>10^4$.

As noted earlier, related P3HT/SiO_2 memory devices ceased operation completely in a vacuum, due mainly to the lack of a redox counterreaction to accompany polythiophene oxidation. When EV is provided to accept electrons as well as provide mobile ClO_4^- ions, memory operation continues after 12 h exposure to vacuum. As shown in Figure 7.19b, the magnitudes of the currents are diminished in vacuum, but the ON/OFF ratio is not significantly affected.[71] Figure 7.20 shows 200 and 2000 W/R/E/R memory cycles performed in vacuum using the same parameters.[34]

Although the magnitudes of the ON and OFF currents decrease with repeated operations, the ON/OFF ratio remains above 50 after 2000 complete cycles. Examination of repeated readout currents in the ON state shows a decrease with time, indicating limited retention, at least for the ON state. This decay is partly due to the recombination reactions of EV^{1+} with PQT^+, resulting in reduction of the conducting polaron state to the initial low conductance neutral form. A separator between the EV and PQT layers that conducts ions but not electrons should greatly reduce or eliminate recombination and extend retention.

Raman spectroscopy provides a means to confirm the memory mechanism, by monitoring the spectrum before and after W/E pulses. The solution spectra of Figure 7.17d show the shift in the prominent band for polythiophene from 1460 to 1405 cm^{-1} when PQT is oxidized to the polaron form, and PQT scattering is sufficiently intense to monitor using a 780 nm laser and commercial spectrometer. As shown in Figure 7.17b, laser illumination could be localized to the S or D

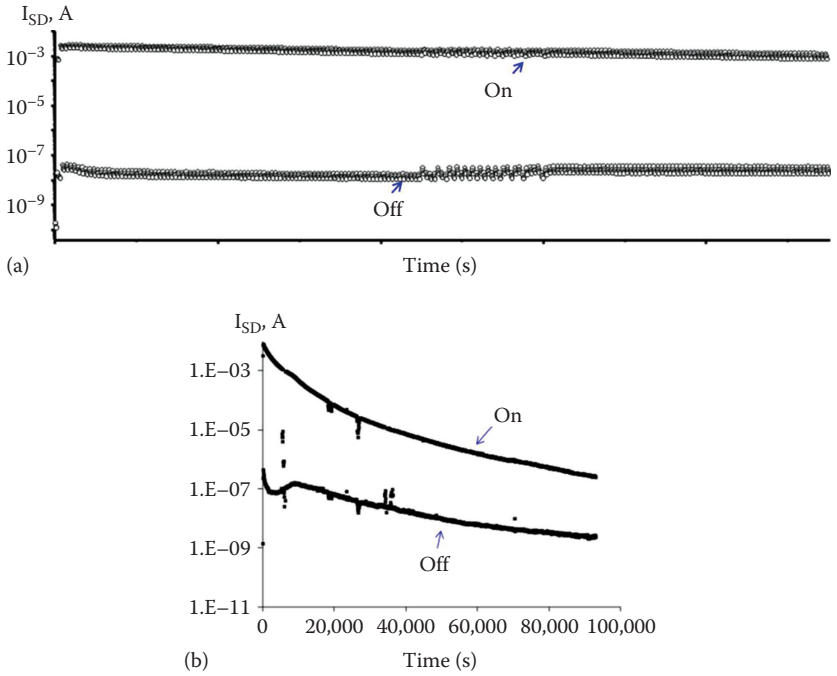

FIGURE 7.20 High (*ON*) and low (*OFF*) currents for V_{SD} = 0.5 V from a PQT/EV–PEO memory device during repetitive R/W/R/E cycles in vacuum for a total of 200 (a) and 2000 (b) cycles. (Used from Das, B.C. et al., *ACS Appl. Mater. Inter.* 5, 11052, 2013. With permission.)

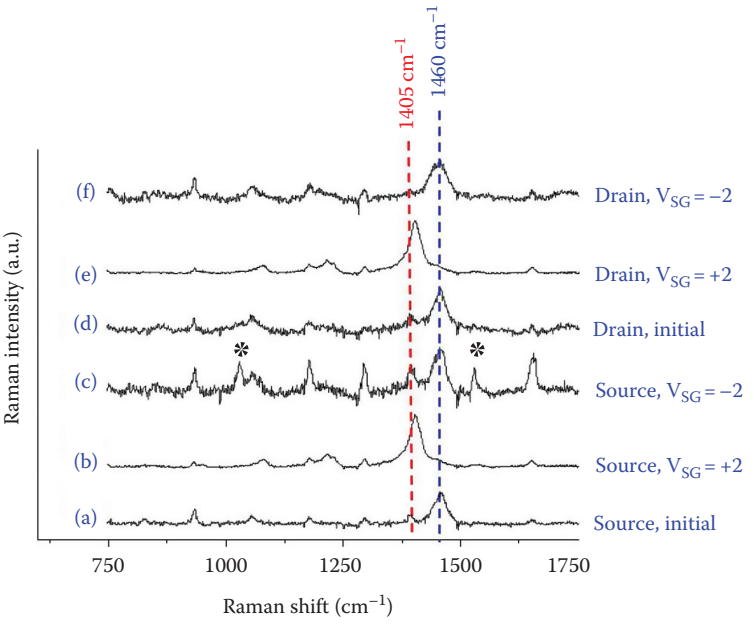

FIGURE 7.21 Raman spectra of a PQT/PEO-EV memory device during operation, over the source and drain regions, as described in the text. (Used from Kumar, R. et al., *J. Am. Chem. Soc.*, 134, 14869, 2012. With permission.)

regions adjacent to the G electrode, or sampling could occur through a G electrode that was partially transparent.

The spectra of Figure 7.21 were obtained at the S and D positions, before and after W and E pulses, with *initial* designating a fresh device not exposed to any bias voltages.[71] Spectra (a) and (d) were obtained at the source and drain electrodes, respectively, for the initial device and show the prominent 1460 cm^{-1} band of the neutral PQT in addition to some small bands related to EV. Spectrum (b) was obtained over the S electrode with V_{SD} = +2 V and demonstrates a shift of the 1460 band to 1405 cm^{-1}, indicating formation of the PQT^{+} polaron at the source. The Raman spectra independently confirm the expected formation of PQT^{+} by a W pulse, consistent with the proposed memory mechanism and associated voltammetry. A similar shift was also observed over the D electrode (spectrum e), which was not expected since the D electrode was not in the SG circuit and could not itself generate PQT^{+}.

Since Raman sampling may occur at various positions on the memory cell structure, it is possible to determine the spatial distribution of structural changes during operation. The main question in the case of the PQT/EV device is the distribution of the conducting PQT^{+} polaron, particularly over the channel. Since the gap region between the S and D electrodes determines the conductance for the *read* process, it is important to know how fast the channel is oxidized. For this purpose, the Raman laser passed through a microscope objective to generate a 3 μm diameter spot, which could be incrementally moved along the path indicated by the dashed white line in Figure 7.22a. A Raman spectrum was obtained at 15 points along the white line, covering S, D, and gap regions, with the results displayed as false color images in Figure 7.22.[71]

Panel B shows the initial image, with Raman shift along the abscissa, position on the ordinate and intensity as false color (with red most intense and dark blue weakest). The red spots show the main PQT band at 1460 cm^{-1}, where it is not attenuated by the gate electrode. Since the gate is e-carbon and Au, it attenuates both the incident laser and the Raman scattering, significantly reducing the apparent Raman intensity. However, it is clear that the PQT is distributed vertically over the S–G–D

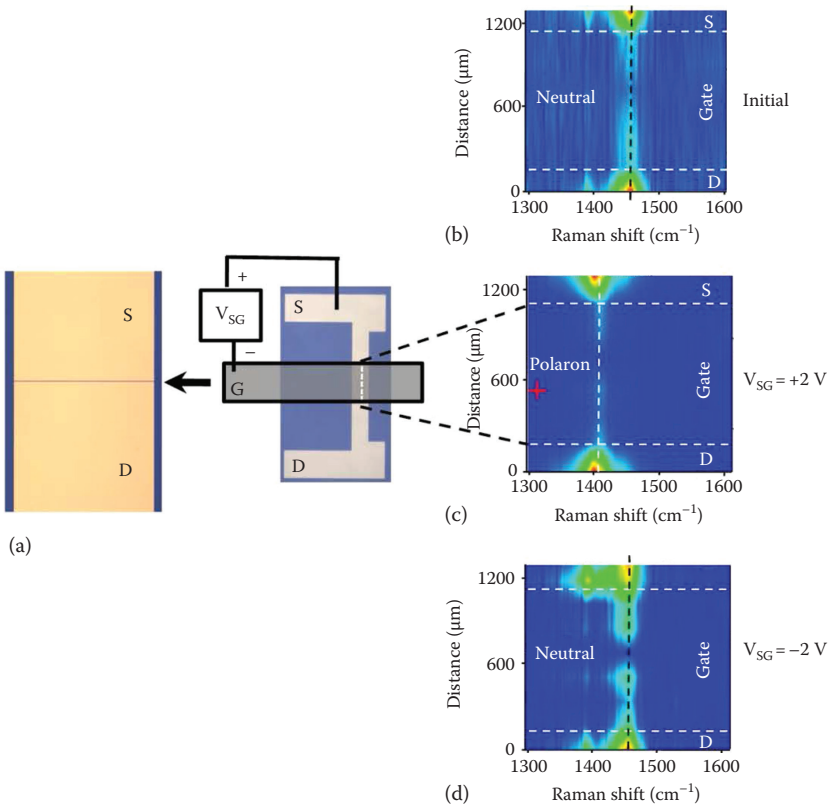

FIGURE 7.22 Spatially resolved Raman images of a PQT/EV–PEO memory device compiled from 15 individual spectra obtained along the line between the S and D electrodes, as shown by the dashed white line in panel (a). Each image shows Raman shift along the abscissa and position on the ordinate, with Raman intensity in false color (red highest). (b) is the initial image, (c) is with V_{SG} = +2 V, and (d) is with V_{SG} = −2 V. (Used from Kumar, R. et al., *J. Am. Chem. Soc.*, 134, 14869, 2012. With permission.)

regions in its neutral, initial form, as expected for an unperturbed device. Figure 7.22c shows an identical scan performed after imposing V_{SG} = +2 V. Within the sampling time of the Raman system (a few seconds), the PQT band shifts from 1460 to 1405 cm^{-1} over the S and D electrodes, both the exposed regions and those under the gate. Recall that the D electrode is not part of the SG circuit and has no bias applied during the entire experiment. Figure 7.22d shows a third scan after V_{SG} was set to −2 V, showing nearly complete return to the initial PQT spectrum. Although the 1 μm wide gap between S and D is not well resolved by the 3 μm Raman sampling region, it is clear that the entire region under the gate and on the D electrode is undergoing oxidation to the conducting PQT^{+} polaron, even though the gap and D electrode are not electrically connected to the external circuit.

A mechanism that accounts for the unexpected oxidation of PQT over the D electrode is shown in Figure 7.23 and depends on the fact that PQT becomes a conductor when it is oxidized to PQT^{+}. Figure 7.23a shows the device shortly after initiation of the *write* pulse, with "N" designating neutral PQT, EV^{2+} the initial oxidized form of EV, and A^{-} the perchlorate anion. Application of a sufficiently positive V_{SG} bias generates PQT^{+} polaron (P^{+}) at the S electrode, which is accompanied by migration of the perchlorate anion into the PQT layer to compensate the polaron charge. Since PQT is both a redox polymer and a conducting polymer (in the PQT^{+} state), it is possible for ET to occur from a nearby neutral molecule to one of the polarons generated at the S electrode, as shown in Figure 7.23b.

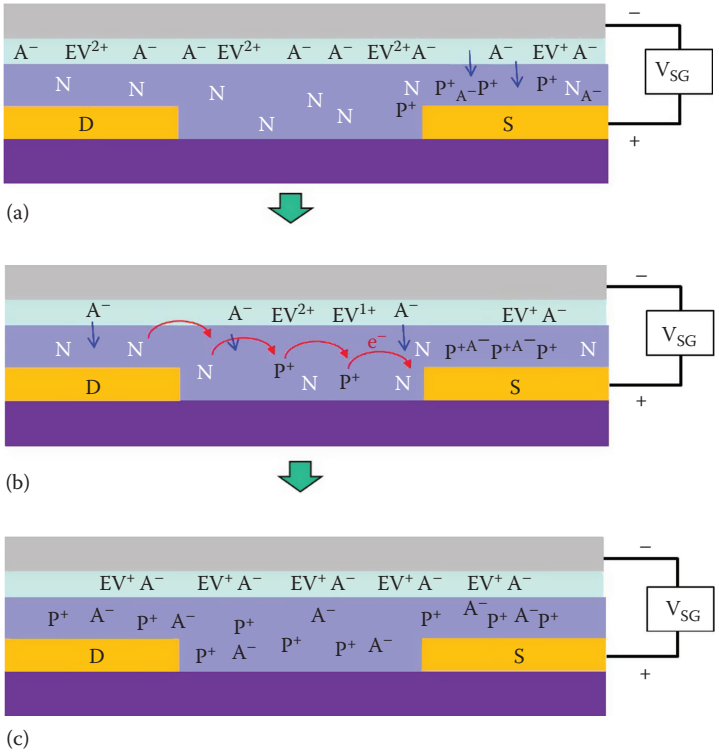

FIGURE 7.23 Schematic of the *write* process, with N = neutral PQT, P^+ = PQT^+ polaron, EV = ethyl viologen, and A^- = perchlorate ion. (a) Immediately after initiation of the write pulse, (b) during polaron propagation across the SD gap, and (c) after complete oxidation of PQT. See text for details.

Such redox exchange reactions occurring in bulk redox polymers have been investigated intensely, and the redox process can extend through micrometer-thick films between two electrodes.[5,6] For the PQT/EV memory device, propagation of the polaron extends into the gap between S and D, and oxidation of the neutral polymer continues until the entire channel and Drain regions are fully oxidized to a conducting film. In effect, the S electrode is increasing in size, as it generates a conducting *front* in the polymer that continues to oxidize PQT to form polarons. Perchlorate ions continue to enter the PQT film from PEO as PQT is oxidized, and such transport may occur anywhere along the axis between the S and D electrodes. As shown in Figure 7.23c, PQT oxidation is accompanied by EV^{2+} reduction, with the end result being a *charged battery* with laterally homogeneous layers and an electronically conducting region between the S and D electrodes. Although the *erase* process with S polarized negatively follows the reverse process to regenerate the initial PQT and EV^{2+} layers, the reduction is less complete due to the loss of conductivity of the PQT^+ film as it is reduced.

We refer to the memory mechanism just described as *redox-gated* organic memory, to highlight the control of SD conductance by an electrochemical reaction. It is clearly an example of solid-state electrochemistry, with the added feature of a second circuit to measure changes in the conductivity of one of the phases. The similarity in geometry to an OFET can be misleading, since the mechanism of operation is fundamentally different in the two devices. The gate bias in an OFET generates charge carriers electrostatically by charging the capacitance between the gate and the S–D electrodes. There is no intentional motion of ions, and the conductance change vanishes as soon as the gate bias is removed. This process is often called *electrostatic doping*, and it may generate the same conducting polarons as the electrochemical analog. But electrostatic doping is not useful for memory devices, since the conductance change induced electrostatically reverts to its initial state

immediately upon removal of the gate bias. Related OFET devices include *electrolyte-gated* FETs, in which mobile ions are used to enhance electrostatic generation of carriers (such as polarons).[95–98] Such devices do not include a redox counterreaction, and the conductance is modified only when the gate bias is present. In redox-gated memory devices, ion motion and a redox counterreaction stabilize the conducting form, resulting in retention of the conductance change for ~30 min after a 1 s *write* pulse for the devices shown in Figure 7.23. For redox gating, the W/E speed depends on the rate of the redox reactions and the motion of counterions, and retention is determined by recombination reactions between the oxidized and reduced products of the *write* reactions. The motion of ions and the associated stabilization of the conducting polaron is the main distinction between a *redox-gated* memory device and an *electrolyte-gated* OFET.

Several basic concepts from electrochemistry are relevant to the performance of redox-gated memory devices and provide guidance for improving speed and retention. The EV^{2+} electron acceptor is essential, since without it, the PQT cannot be oxidized. As was the case with SiO_2 devices, adventitious H_2O can act as a receptor, but replacement of EV–PEO with PEO containing $LiClO_4$ and residual H_2O causes memory operation to cease completely in a vacuum. As shown in Figure 7.24, the active polymer must be both redox active and have high and low conductivity states, since replacement of PQT with poly(vinyl-ferrocene) (PVFc) results in an ON/OFF ratio four orders of magnitude lower than that of PQT or P3HT.

The small conductance change observed with PVFc is likely due to redox exchange current between the S and D electrodes[5,6] and is much smaller than the dc conduction through the PQT polaron. Not surprisingly, replacement of the PQT with polystyrene that is neither redox active nor conducting results in a very small observable conductance change.

The dynamics of the *write* operation were monitored with the circuit shown in Figure 7.25a, which amounts to a bipotentiostat familiar to electrochemists. The S electrode is biased by the *write* voltage, and the S and D currents are monitored independently and simultaneously. Control of the D voltage permits different bias values for V_{SD} and V_{SG}, and the entire experiment is conducted by a data acquisition system with LabVIEW software. The SG current for PQT and PVFc devices, both containing PEO-EV, is shown in Figure 7.25b for a V_{SG} = +3 V *write* pulse lasting 2 s.[34]

The current magnitudes are comparable for PQT and PVFc, since in both cases, the SG current is oxidizing the polymers and there is little or no dc conduction. The increase in the PQT response with time is likely due to the propagation of polaron away from the S electrode. The SD current response accompanying the PQT *write* pulse for a constant V_{SD} of 0.5 V is shown in Figure 7.25c, overlaid

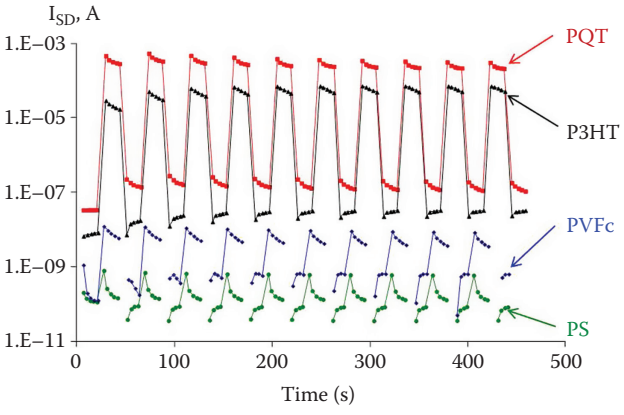

FIGURE 7.24 Ten R/W/R/E memory cycles for polymer/EV–PEO devices that are identical except for the active polymer layer, as indicated. W/E pulses were ±4 V and 1 s long in all cases. PS = polystyrene and PVFc = poly(vinyl ferrocene). (Used from Das, B.C. et al., *ACS Appl. Mater. Inter.*, 5, 11052, 2013. With permission.)

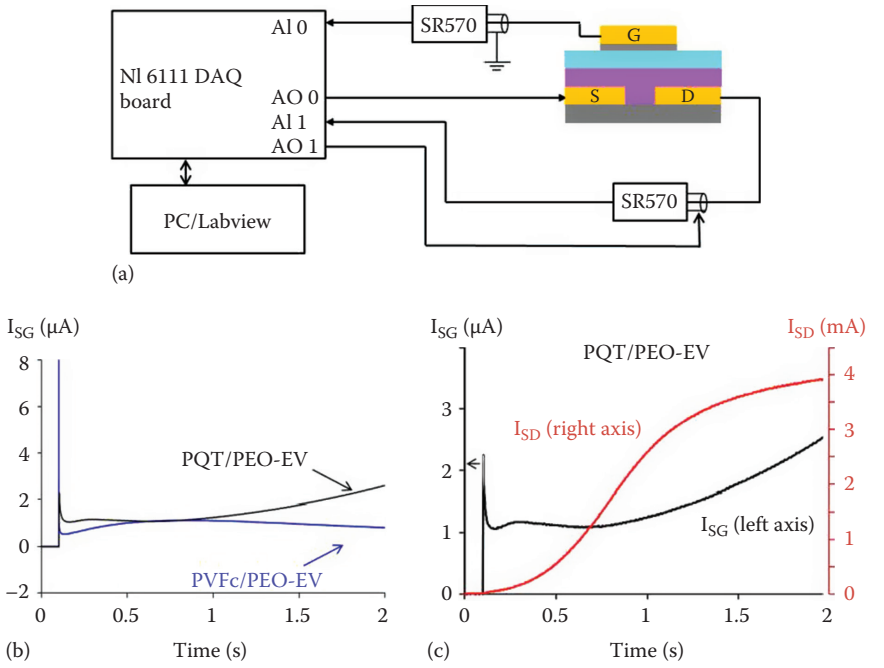

FIGURE 7.25 (a) Schematic for dual pulse experiment permitting simultaneous monitoring of SG and SD circuits. SR570 = Stanford Research current amplifier, NI 6111 = National Instruments data acquisition board. (b) SG current in response to V_{SG} = 3 V *write* pulse for polymer/PEO-EV devices containing different polymers, as indicated. (c) SD and SG currents for PQT/PEO-EV device obtained simultaneously during a 3 V write pulse. Not large difference in current scales. (b and c used from Das, B.C. et al., *ACS Appl. Mater. Inter.*, 5, 11052, 2013. With permission.)

with the SG current recorded simultaneously. Note that the current scales are very different in panel (c), with the SD current increasing to >3 mA, while the SG current remains below 3 μA. There is an effectively large *gain* in the devices, since a small SG current can produce a large SD response due to formation of the conducting PQT^+ layer between S and D. This effect is similar to that observed in *electrochemical transistors* made from conducting polymers in electrolyte solution,[8] except that the present devices are all solid state. The dual pulse experiment of Figure 7.25 provides direct information about the *write* speed of the memory device, as judged by the time required to reach some threshold I_{SD} value. Obviously, a write speed of hundreds of milliseconds is not competitive with commercial memory devices, so the factors controlling write speed need to be determined.

An important clue is provided by the magnitude of the I_{SG} response of Figure 7.25b, which directly indicates the rate of polaron generation at the S electrode and then propagation into the SD gap. A ~ 1 μA SG current is predicted to completely oxidize the PQT between the S and G electrodes in a few 100 ms, approximately the time required to produce a significant I_{SD} response. This inference implies that the rate of polaron formation is simply too slow to rapidly fill the SG or SD regions and must be increased to improve *write* speed. Figure 7.26 shows the strong effect of local atmosphere on device speed, for a single device that was first run in air, then after 12 h in vacuum ($<1 \times 10^{-5}$ torr), and then after admitting acetonitrile vapor into the vacuum chamber. Note that the vacuum removes most of the water from the device, which should not only prevent its possible redox reactions but also reduce ionic conductivity.

An acetonitrile atmosphere with no added water vapor shows much faster *write* speed, and much higher I_{SG}, indicating more rapid formation of polarons. These results are consistent with device speed controlled by ion transport, which must accompany PQT^+ formation. Both water

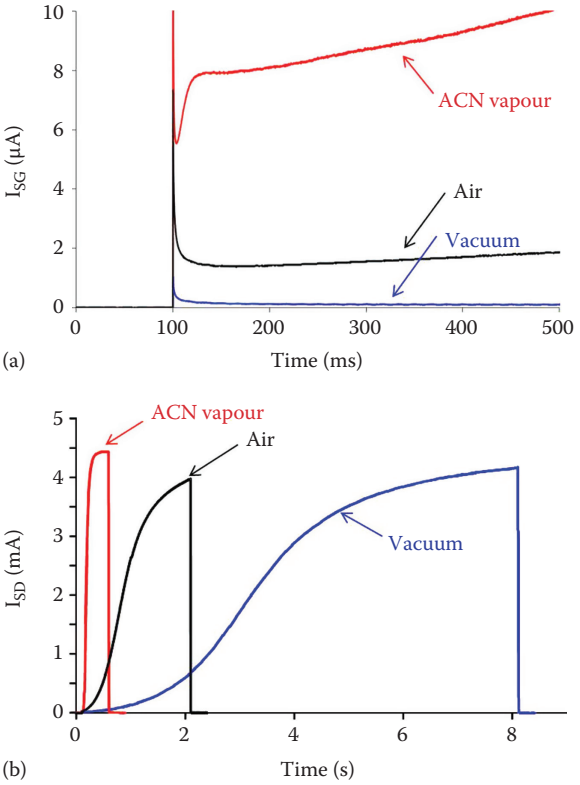

FIGURE 7.26 Effect of atmosphere on (a) SG and (b) SD current responses for a PQT/PEO-EV memory device during a V_{SG} = +3 V pulse, initially in air, then after 12 h in vacuum, and then again after 10 min in acetonitrile vapor in the same vacuum chamber. Duration of the V_{SG} in panel B due to the varying device response speeds. (Used from Das, B.C. et al., *ACS Appl. Mater. Inter.*, 5, 11052, 2013. With permission.)

and acetonitrile can stabilize mobile ions in the PEO (and presumably in PQT), thus reducing the ohmic losses in the cell during *write* operations.[34] These losses can be partially overcome with an increased V_{SG} and can be used to advantage. Figure 7.27 shows not only that increased V_{SG} causes higher conductance for a given *write* time, but also that different conductance states are possible and repeatable.[34] The prospect of *multistate memory* increases the effective data density and has been considered for many solid-state devices but never achieved commercially. Control of conductance by *write* voltage is at least a conceivable mechanism for increasing storage capacity in redox-gated memory devices.

The PQT/EV memory devices are currently deficient in both W/E speed and retention, but appreciation of the mechanism provides a *road map* for improvement, as well as quantitative indications of what performance is ultimately possible. The conductivity of ClO_4^- is approximately 10^{-7} S cm^{-1} in PEO, determined from the PQT/EV devices. Solid-state electrolytes vary greatly in ionic conductivity, but many examples have conductivities above 0.01 S cm^{-1}. Implementation of one of these electrolytes to conduct anions could decrease *write* time by up to five orders of magnitude. Furthermore, incorporation of acetonitrile in solid-state electronic devices is not impractical, given the wide use of carbonate solvents in lithium batteries. As already noted, a second parameter of direct interest to practical applications is retention time, which must be much greater than that of DRAM (<100 ms) and approach today's *flash* (>10 years). The redox-gated devices described here lack separators, so recombination is expected and responsible for the short retention time of several minutes. But adding an ionic conductor that is electronically insulating between the PQT and EV layers should in

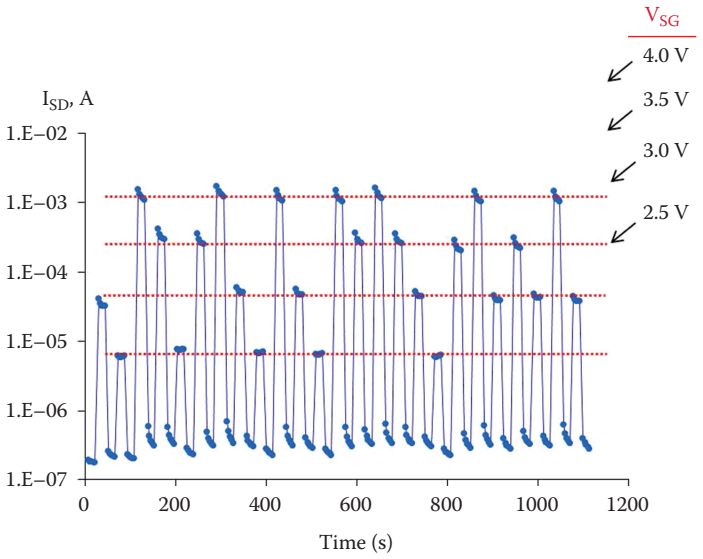

FIGURE 7.27 Demonstration of five distinct conductance states for a single PQT/PEO-EV memory in response to random application of four different V_{SG} pulses. V_{SD} was 0.5 V in all cases. (Used from Das, B.C. et al., *ACS Appl. Mater. Inter.*, 5, 11052, 2013. With permission.)

principle extend retention indefinitely by preventing recombination. Mechanistically, retention is analogous to *shelf life* in common batteries, and those can easily exceed 10 years. The potentially low W/E energy requirement of redox gating combined with better cycle life than current *flash* memory provides the incentive for further improvements in performance of redox-gated devices.

7.5 CONCLUSIONS AND FUTURE PROSPECTS

This chapter explored relationships between electrochemical phenomena and the behavior of nanoscopic layers of molecules in microelectronic devices. Some useful generalizations about ME are available, which will likely continue to be significant as the field develops. First, a modified electrode or a MJ must be considered as one electronic system, with properties quite different from those of the isolated electrode material and unbound molecules. The strong electronic coupling discussed in Section 7.3 significantly affects electronic properties such as transport and tunneling barriers and must be considered when designing molecular electronic devices. A visual demonstration of electronic coupling is provided in Figure 7.28, which shows the molecular orbitals for a NAB molecule bonded to a nine-ring graphene molecule (G9). G9 is used to model the sp^2 lattice in the PPF electrode and the entire system is optimized, yielding a low-energy dihedral angle between the G9 and NAB of 37°.

The HOMO is localized on G9, while the next highest occupied orbital (HOMO-1) has electron density on both the G9 and NAB. One consequence of the sharing of electrons between the G9 and NAB is the *leveling effect* noted in Figure 7.12, and strong coupling is clearly an important factor in choosing molecules and surface bonding schemes for MJs.[13,78] It is likely that theoretical methods such as density functional theory will be critical for the design and understanding of practical ME, once the structural factors affecting transport are understood.

A second important observation is that tunneling is not the only transport mechanism mediating electron transport in MJs. As noted in Section 7.1, electron transport across >100 nm distances in organic semiconductors has been studied extensively and is generally considered a hopping mechanism by redox exchange, variable range hopping, etc. Figure 7.29 shows tunneling and hopping at the short and long extremes of the scale of transport distances relevant to solid-state electronics.

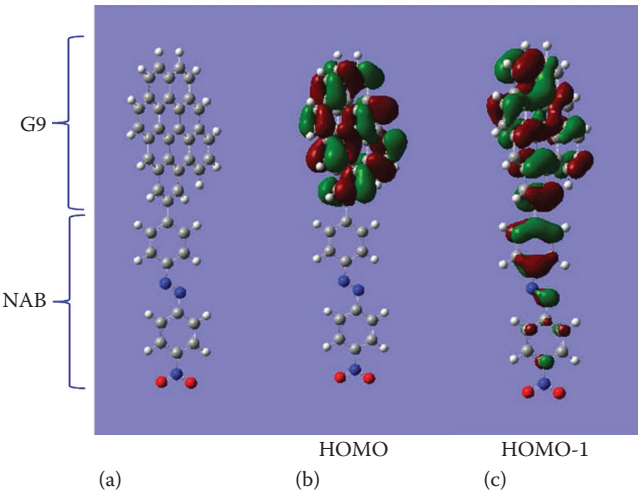

FIGURE 7.28 (a) Structure of graphene–NAB model compound used to calculate orbitals for NAB bonded to PPF. Optimized structure has a dihedral angle between G9 and NAB of 37°. (b) HOMO orbital for the G9–NAB system, calculated with Gaussian 09[99] B3LYP 6-31G(d). (c) HOMO-1 orbital, showing distribution of electron density over both G9 and NAB.

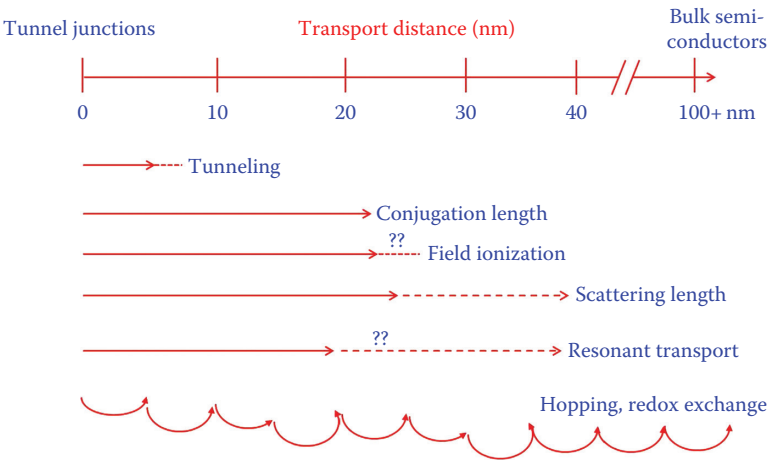

FIGURE 7.29 Transport phenomena in molecular and organic devices ranging from tunnel junctions to bulk semiconductors (upper scale). Arrows indicate the length scales of various effects, with the dashed lines indicating uncertainty. (Adapted from McCreery, R. et al., *Phys. Chem. Chem. Phys.*, 15, 1065, 2013. With permission.)

Hopping across >100 nm is temperature dependent due to reorganization associated with redox exchange and often leads to low carrier mobility. As discussed in Section 7.3, transport by tunneling can extend for 5–8 nm for aromatic molecules, and the range of possible tunneling barriers is compressed by the leveling effect of strong electronic coupling. However, Figure 7.14 shows at least one additional mechanism between tunneling and redox exchange that is effective at least over the range of 8–22 nm, which is consistent with field ionization. As indicated in Figure 7.29, conjugation length can exceed 10 nm and raises the possibility that a single molecular orbital can bridge between

the two contacts. *Resonant* transport should occur when a molecular orbital of the contact/molecule/contact electronic system has an energy close to the contact Fermi level. The possible range of distances for resonant transport is not known, but is likely equal to or greater than the conjugation length and may resemble band transport in metals. Note that field ionization and resonant transport do not necessarily involve redox exchange and may be much more efficient than the *hopping* in bulk organic semiconductors. Note also that transport through >20 nm is likely possible without scattering, hence could be *ballistic*, that is, very fast, with lower power and heat dissipation demands than current microelectronic devices.

As described in Section 7.4, solid-state redox reactions can affect device behavior and are useful for creating two or more metastable states in molecular memory devices. Such reactions are controlled by many of the same phenomena as solution electrochemistry, notably activated ET, and charge compensation by ion motion. It is likely that less conventional redox events can occur in MJs, such as reorganization of a conjugated molecule during electron or hole transport through it.[82,100,101] The term *nanoionics* has been used to describe ion motion across nanoscopic dimensions, notably in memory devices.[102–104] Although the mobility of ions in solid-state devices can be low, the transport distances involved are often very short, and the ion transport time can easily be in the nanosecond to microsecond range. Ion transport and redox reactions are unlikely (and usually avoided) in conventional microelectronic devices and provide avenues to novel electronic behavior not currently possible.

After an initial burst of excitement over the prospect of molecules acting as circuit elements, we might consider the prospects of ME for practical integration in widely used microelectronic products. A prerequisite to such adoption is the requirement for compatibility with processing techniques and temperature excursions common to microelectronic manufacturing, as it appears likely that ME will be used initially in hybrid devices with conventional semiconductors. The existing industry is sophisticated and well established, so augmentation by integration of molecular devices is much more likely than replacement of silicon. The main driving force for the adoption of ME in the real world will be novel functions and properties not currently possible with silicon. Resonant transport, field ionization, redox reactions, ion motion, and chemical recognition are phenomena that are possible in molecular electronic systems that are not readily achieved with silicon. Assuming that these or other functions become possible with ME and yield new types of electronic devices, the additional processing concerns associated with integration of molecules in microelectronic manufacturing will likely be addressed readily.

ACKNOWLEDGMENTS

The author's work described in this chapter was supported by the National Research Council (Canada), the Natural Science and Engineering Research Council, the University of Alberta, and Alberta Innovates Technology Futures. The author thanks Bryan Szeto and Nikola Pekas for fabrication expertise and Adam Bergren and Haijun Yan for many useful discussions.

REFERENCES

1. Smalley, J. F., Finklea, H. O., Chidsey, C. E. D. et al. 2003 Heterogeneous electron-transfer kinetics for ruthenium and ferrocene redox moieties through alkanethiol monolayers on gold. *J. Am. Chem. Soc.* 125:2004–2013.
2. Sikes, H. D., Smalley, J. F., Dudek, S. P. et al. 2001 Rapid electron tunneling through oligophenylenevinylene bridges. *Science* (Washington, DC) 291:1519–1523.
3. Creager, S., Yu, C. J., Bamdad, C. et al. 1999 Electron transfer at electrodes through conjugated "Molecular Wire" bridges. *J. Am. Chem. Soc.* 121:1059–1064.
4. Finklea, H. O. 1996 Electrochemistry of organized monolayers of thiols and related molecules on electrodes. *Electroanalytical Chemistry*, ed Bard AJ (Dekker, New York), Vol. 19, pp. 109–335.

5. Sullivan, M. G. and Murray, R. W. 1994 Solid state electron self-exchange dynamics in mixed valent poly(vinylferrocene) films. *J. Phys. Chem.* 98:4343–4351.
6. Daum, P., Lenhard, J. R., Rolison, D., and Murray, R. W. 1980 Diffusional charge transport through ultrathin films of radiofrequency plasma polymerized vinylferrocene at low temperature. *J. Am. Chem. Soc.* 102:4649–4653.
7. Buttry, D. A. and Anson, F. C. 1983 Effects of electron exchange and single-file diffusion on charge propagation in nafion films containing redox couples. *J. Am. Chem. Soc.* 105:685–689.
8. Ofer, D., Crooks, R. M., and Wrighton, M. S. 1990 Potential dependence of the conductivity of highly oxidized polythiophenes, polypyrroles, and polyaniline: Finite windows of high conductivity. *J. Am. Chem. Soc.* 112:7869–7879.
9. Heath, J. R. and Ratner, M. A. 2003 Molecular electronics. *Phys. Today* 56:43–49.
10. Jortner, J. and Ratner, M. 1997 *Molecular Electronics* (Blackwell Science Ltd., Maiden, MA), p. 485.
11. Mirkin, C. A. and Ratner, M. A. 1992 Molecular electronics. *Annu. Rev. Phys. Chem.* 43:719–754.
12. Lindsay, S. M. and Ratner, M. A. 2007 Molecular transport junctions: Clearing mists. *Adv. Mater.* 19:23–31.
13. McCreery, R., Yan, H., and Bergren, A. J. 2013 A critical perspective on molecular electronic junctions: There is plenty of room in the middle. *Phys. Chem. Chem. Phys.* 15:1065–1081.
14. McCreery, R. L. and Bergren, A. J. 2009 Progress with molecular electronic junctions: Meeting experimental challenges in design and fabrication. *Adv. Mater*. 21:4303–4322.
15. McCreery, R. 2004 Molecular electronic junctions. *Chem. Mat.* 16:4477–4496.
16. Chen, F. and Tao, N. J. 2009 Electron transport in single molecules: From benzene to graphene. *Acc. Chem. Res*. 42:429–438.
17. Huang, Z. F., Chen, F., Bennett, P. A., and Tao, N. J. 2007 Single molecule junctions formed via Au-Thiol contact: Stability and breakdown mechanism. *J. Am. Chem. Soc.* 129:13225–13231.
18. Tao, N. J. 2006 Electron transport in molecular junctions. *Nat. Nanotechnol.* 1:173.
19. Caldwell, M. A., Jeyasingh, R. G. D., Wong, H. S. P., and Milliron, D. J. 2012 Nanoscale phase change memory materials. *Nanoscale* 4:4382–4392.
20. Heremans, P., Gelinck, G. H., Muller, R. et al. 2011 Polymer and organic nonvolatile memory devices. *Chem. Mater.* 23:341–358.
21. Chih-Yuan, L. and Kuan, H. 2009 Nonvolatile semiconductor memory revolutionizing information storage. *IEEE Nanotechnol. Mag.* 3:4–9.
22. Scott, J. C. and Bozano, L. D. 2007 Nonvolatile memory elements based on organic materials. *Adv. Mater.* 19:1452–1463.
23. Kuhr, W. G. 2004 Integration of molecular components into silicon memory devices. *Interface (The Electrochemical Society)* 13:34–38.
24. Waser, R., Dittmann, R., Staikov, G., and Szot, K. 2009 Redox-based resistive switching memories—Nanoionic mechanisms, prospects, and challenges. *Adv. Mater.* 21:2632–2663.
25. Strukov, D. B., Snider, G. S., Stewart, D. R., and Williams, R. S. 2008 The missing memristor found. *Nature* 453:80–83.
26. Wu, J. and McCreery, R. L. 2009 Solid-state electrochemistry in molecule/TiO_2 molecular heterojunctions as the basis of the TiO_2 "Memristor". *J. Electrochem. Soc.* 156:P29–P37.
27. Lee, M.-J., Lee, C. B., Lee, D. et al. 2011 A fast, high-endurance and scalable non-volatile memory device made from asymmetric $Ta_2O_{5a'x}/TaO_{2a'x}$ bilayer structures. *Nat. Mater.* 10:625–630.
28. Roth, K. M., Yasseri, A. A., Liu, Z. et al. 2003 Measurements of electron-transfer rates of charge-storage molecular monolayers on Si(100). Toward hybrid molecular/semiconductor information storage devices. *J. Am. Chem. Soc.* 125:505–517.
29. Wei, D., Baral, J. K., Osterbacka, R., and Ivaska, A. 2008 Electrochemical fabrication of a nonvolatile memory device based on polyaniline and gold particles. *J. Mater. Chem.* 18:1853–1857.
30. Chauhan, A. K., Aswal, D. K., Koiry, S. P. et al. 2008 Resistive memory effect in self-assembled 3-aminopropyltrimethoxysilane molecular multilayers. *Phys. Status Solid A* 205:373–377.
31. Frank, V., Stefan, C. J. M., Rene, A. J. J. et al. 2007 Reproducible resistive switching in nonvolatile organic memories. *Appl. Phys. Lett.* 91:192103.
32. Kim, D. C., Seo, S., Ahn, S. E. et al. 2006 Electrical observations of filamentary conductions for the resistive memory switching in NiO films. *Appl. Phys. Lett.* 88:202102.
33. Kozicki, M. N., Park, M., and Mitkova, M. 2005 Nanoscale memory elements based on solid-state electrolytes. *IEEE Trans. Nanotechnol*. 4:331–338.
34. Haick, H., Niitsoo, O., Ghabboun, J., and Cahen, D. 2007 Electrical contacts to organic molecular films by metal evaporation: Effect of contacting details. *J. Phys. Chem. C* 111:2318–2329.

35. Kim, B., Choi, S. H., Zhu, X. Y., and Frisbie, C. D. 2011 Molecular tunnel junctions based on pi-conjugated oligoacene thiols and dithiols between Ag, Au, and Pt contacts: Effect of surface linking group and metal work function. *J. Am. Chem. Soc.* 133:19864–19877.
36. Kim, B., Beebe, J. M., Jun, Y., Zhu, X. Y., and Frisbie, C. D. 2006 Correlation between HOMO alignment and contact resistance in molecular junctions: Aromatic thiols versus aromatic isocyanides. *J. Am. Chem. Soc.* 128:4970–4971.
37. Bergren, A. J., McCreery, R. L., Stoyanov, S. R., Gusarov, S., and Kovalenko, A. 2010 Electronic characteristics and charge transport mechanisms for large area aromatic molecular junctions. *J. Phys. Chem. C* 114:15806–15815.
38. McCreery, R., Wu, J., and Kalakodimi, R. J. 2006 Electron transport and redox reactions in carbon based molecular electronic junctions. *Phys. Chem. Chem. Phys*. 8:2572–2590.
39. Ranganathan, S., McCreery, R. L., Majji, S. M., and Madou, M. 2000 Photoresist-derived carbon for microelectrochemical applications. *J. Electrochem. Soc*. 147:277–282.
40. Ranganathan, S. and McCreery, R. L. 2001 Electroanalytical performance of carbon films with near-atomic flatness. *Anal. Chem.* 73:893–900.
41. Kostecki, R., Song, X., and Kinoshita, K. 1999 Electrochemical analysis of carbon interdigitated microelectrodes. *Electrochem. Solid State Lett.* 2:465.
42. Fairman, C., Yu, S., Liu, G. et al. 2008 Exploration of variables in the fabrication of pyrolysed photoresist. *J. Solid State Electrochem*. 12:1357–1365.
43. Bergren, A. J. and McCreery, R. L. 2011 Analytical chemistry in molecular electronics. *Annu. Rev. Anal. Chem.* 4:173–195.
44. Ru, J., Szeto, B., Bonifas, A., and McCreery, R. L. 2010 Microfabrication and integration of diazonium-based aromatic molecular junctions. *ACS Appl. Mater. Inter.* 2:3693–3701.
45. Belanger, D. and Pinson, J. 2011 Electrografting: A powerful method for surface modification. *Chem. Soc. Rev.* 40:3995–4048.
46. Lehr, J., Garrett, D. J., Paulik, M. G. et al. 2010 Patterning of metal, carbon, and semiconductor substrates with thin organic films by microcontact printing with aryldiazonium salt inks. *Anal. Chem.* 82:7027–7034.
47. Garrett, D. J., Lehr, J., Miskelly, G. M., and Downard, A. J. 2007 Microcontact printing using the spontaneous reduction of aryldiazonium salts. *J. Am. Chem. Soc.* 129:15456–15457.
48. Pinson, J. and Podvorica, F. 2005 Attachment of organic layers to conductive or semiconductive surfaces by reduction of diazonium salts. *Chem. Soc. Rev.* 34:429–439.
49. Brooksby, P. A., Downard, A. J., and Yu, S. S. C. 2005 Effect of applied potential on arylmethyl films oxidatively grafted to carbon surfaces. *Langmuir* 21:11304–11311.
50. Delamar, M., Hitmi, R., Pinson, J., and Saveant, J. M. 1992 Covalent modification of carbon surfaces by grafting of functionalized aryl radicals produced from electrochemical reduction of diazonium salts. *J. Am. Chem. Soc.* 114:5883–5884.
51. Kariuki, J. K. and McDermott, M. T. 2001 Formation of multilayers on glassy carbon electrodes via the reduction of diazonium salts. *Langmuir* 17:5947–5951.
52. Kariuki, J. K. and McDermott, M. T. 1999 Nucleation and growth of functionalized aryl films on graphite electrodes. *Langmuir* 15:6534–6540.
53. Anariba, F., DuVall, S. H., and McCreery, R. L. 2003 Mono- and multilayer formation by diazonium reduction on carbon surfaces monitored with atomic force microscopy "Scratching". *Anal. Chem.* 75:3837–3844.
54. Yan, H., Bergren, A. J., McCreery, R. et al. 2013 Activationless charge transport across 4.5 to 22 nm in molecular electronic junctions. *Proc. Nat. Acad. Sci. U. S. A.* 110:5326–5330.
55. Walker, A. V., Tighe, T. B., Haynie, B. C. et al. 2005 Chemical pathways in the interactions of reactive metal atoms with organic surfaces: Vapor deposition of Ca and Ti on a methoxy-terminated alkanethiolate monolayer on Au. *J. Phys. Chem. B* 109:11263–11272.
56. Walker, A. V., Tighe, T. B., Cabarcos, O. M. et al. 2004 The dynamics of noble metal atom penetration through methoxy-terminated alkanethiolate monolayers. *J. Am. Chem. Soc.* 126:3954–3963.
57. Fisher, G. L., Walker, A. V., Hooper, A. E. et al. 2002 Bond insertion, complexation, and penetration pathways of vapor-deposited aluminum atoms HO- and CH_3O-terminated organic monolayers. *J. Am. Chem. Soc.* 124:5528–5541.
58. Mahmoud, A. M., Bergren, A. J., Pekas, N., and McCreery, R. L. 2011 Towards integrated molecular electronic devices: Characterization of molecular layer integrity during fabrication processes. *Adv. Funct. Mater.* 21:2273–2281.

59. Nowak, A. M. and McCreery, R. L. 2004 In situ Raman spectroscopy of bias-induced structural changes in nitroazobenzene molecular electronic junctions. *J. Am. Chem. Soc.* 126:16621–16631.
60. DeIonno, E., Tseng, H. R., Harvey, D. D., Stoddart, J. F., and Heath, J. R. 2006 Infrared spectroscopic characterization of [2]rotaxane molecular switch tunnel junction devices. *J. Phys. Chem. B* 110:7609–7612.
61. Wang, W., Scott, A., Gergel-Hackett, N. et al. 2008 Probing molecules in integrated silicon-molecule-metal junctions by inelastic tunneling spectroscopy. *Nano Lett.* 8:478–484.
62. Richter, C. A., Hacker, C. A., and Richter, L. J. 2005 Electrical and spectroscopic characterization of metal/monolayer/Si devices. *J. Phys. Chem. B* 109:21836–21841.
63. Hacker, C., Batteas, J. D., Garno, J. C. et al. 2004 Structural and chemical characterization of monofluoro substituted oligo(phenylene-ethynylene) thiolate self-assembled monolayers on gold. *Langmuir* 20:6195–6205.
64. Yan, H., Bergren, A. J., and McCreery, R. L. 2011 All-carbon molecular tunnel junctions. *J. Am. Chem. Soc.* 133:19168–19177.
65. Haynie, B. C., Walker, A. V., Tighe, T. B., Allara, D. L., and Winograd, N. 2003 Adventures in molecular electronics: How to attach wires to molecules. *Appl. Surf. Sci.* 203–204:433–436.
66. Bonifas, A. P. and McCreery, R. L. 2010 "Soft" Au, Pt and Cu contacts for molecular junctions through surface-diffusion-mediated deposition. *Nat. Nanotechnol.* 5:612–617.
67. Bonifas, A. P. and McCreery, R. L. 2011 Assembling molecular electronic junctions one molecule at a time. *Nano Lett.* 11:4725–4729.
68. Pan, H., Li, Y., Wu, Y. et al. 2007 Low-temperature, solution-processed, high-mobility polymer semiconductors for thin-film transistors. *J. Am. Chem. Soc.* 129:4112–4113.
69. Wu, Y., Liu, P., Ong, B. S. et al. 2005 Controlled orientation of liquid-crystalline polythiophene semiconductors for high-performance organic thin-film transistors. *Appl. Phys. Lett.* 86:142102–142103.
70. Ong, B. S., Wu, Y., Liu, P., and Gardner, S. 2004 High-performance semiconducting polythiophenes for organic thin-film transistors. *J. Am. Chem. Soc.* 126:3378–3379.
71. Kumar, R., Pillai, R. G., Pekas, N., Wu, Y., and McCreery, R. L. 2012 Spatially resolved Raman spectroelectrochemistry of solid-state polythiophene/viologen memory devices. *J. Am. Chem. Soc.* 134:14869–14876.
72. Shoute, L. C. T., Wu, Y., and McCreery, R. L. 2013 Direct spectroscopic monitoring of conductance switching in polythiophene memory devices. *Electrochim. Acta* 110:437–445.
73. Shoute, L., Pekas, N., Wu, Y., and McCreery, R. 2011 Redox driven conductance changes for resistive memory. *Appl. Phys A: Mater Sci. Process.* 102:841–850.
74. Yang, H.-H. and McCreery, R. L. 1999 Effects of surface monolayers on the electron transfer kinetics and adsorption of methyl viologen and phenothiazine derivatives on glassy carbon electrodes. *Anal. Chem.* 71:4081–4087.
75. Simmons, J. G. 1964 Generalized thermal J-V characteristic for the electric tunnel effect. *J. Appl. Phys.* 35:2655–2658.
76. Simmons, J. G. 1963 Generalized formula for the electric tunnel effect between similar electrodes separated by a thin insulating film. *J. Appl. Phys.* 34:1793–1803.
77. Simmons, J. G. 1963 Electric tunnel effect between dissimilar electrodes separated by a thin insulating film. *J. Appl. Phys.* 34:2581–2590.
78. Sayed, S. Y., Fereiro, J. A., Yan, H., McCreery, R. L., and Bergren, A. J. 2012 Charge transport in molecular electronic junctions: Compression of the molecular tunnel barrier in the strong coupling regime. *Proc. Natl. Acad. Sci. U. S. A.* 109:11498–11503.
79. Har-Lavan, R., Yaffe, O., Joshi, P. et al. 2012 Ambient organic molecular passivation of Si yields near-ideal, Schottky-Mott limited, junctions. *AIP Adv.* 2:012164.
80. Koch, N. and Vollmer, A. 2006 Electrode-molecular semiconductor contacts: Work-function-dependent hole injection barriers versus Fermi-level pinning. *Appl. Phys. Lett.* 89:162107–162113.
81. Simmons, J. G. 1964 Potential barriers and emission-limited current flow between closely spaced parallel metal electrodes. *J. Appl. Phys.* 35:2472–2481.
82. Burin, A. L., Berlin, Y. A., and Ratner, M. A. 2001 Semiclassical theory for tunneling of electrons interacting with media. *J. Phys. Chem. A* 105:2652–2659.
83. Buttiker, M. and Landauer, R. 1982 Traversal time for tunneling. *Phys. Rev. Lett.* 49:1739.
84. Fereiro, J. A., McCreery, R. L., and Bergren, A. J. 2013 Direct optical determination of interfacial transport barriers in molecular tunnel junctions. *J. Am. Chem. Soc.* 135:9584–9587.
85. Hwang, J., Wan, A., and Kahn, A. 2009 Energetics of metal–organic interfaces: New experiments and assessment of the field. *Mater. Sci. Eng.: R: Reports* 64:1–31.

86. Salomon, A., Shpaisman, H., Seitz, O., Boecking, T., and Cahen, D. 2008 Temperature-dependent electronic transport through alkyl chain monolayers: Evidence for a molecular signature. *J. Phys. Chem. C* 112:3969–3974.
87. Haick, H. and Cahen, D. 2008 Making contact: Connecting molecules electrically to the macroscopic world. *Prog. Surf. Sci.* 83:217–261.
88. Sze, S. M. 1981 *Physics of Semiconductor Devices* (Wiley, New York) 2nd edn.
89. Bonifas, A. P. and McCreery, R. L. 2012 Solid state spectroelectrochemistry of redox reactions in polypyrrole/oxide molecular heterojunctions. *Anal. Chem.* 84:2459–2465.
90. Barman, S., Deng, F., and McCreery, R. 2008 Conducting polymer memory devices based on dynamic doping. *J. Am. Chem. Soc.* 130:11073–11081.
91. Strachan, J. P., Pickett, M. D., Yang, J. J. et al. 2010 Direct identification of the conducting channels in a functioning memristive device. *Adv. Mater.* 22:3573–3577.
92. Strukov, D. B. and Williams, R. S. 2009 Exponential ionic drift: Fast switching and low volatility of thin-film memristors. *Appl. Phys. A: Mater. Sci. Process.* 94:515–519.
93. Gergel-Hackett, N., Hamadani, B., Dunlap, B. et al. 2009 A flexible solution-processed memristor. *IEEE Electr. Device Lett.* 30:706–708.
94. Das, B. C., Pillai, R. G., Wu, Y., and McCreery, R. L. 2013 Redox-gated three-terminal organic memory devices: Effect of composition and environment on performance. *ACS Appl. Mater. Inter.* 5:11052–11058.
95. Herlogsson, L., Noh, Y.-Y., Zhao, N. et al. 2008 Downscaling of organic field-effect transistors with a polyelectrolyte gate insulator. *Adv. Mater.* 20:4708–4713.
96. Kaake, L. G., Zou, Y., Panzer, M. J., Frisbie, C. D., and Zhu, X. Y. 2007 Vibrational spectroscopy reveals electrostatic and electrochemical doping in organic thin film transistors gated with a polymer electrolyte dielectric. *J. Am. Chem. Soc.* 129:7824–7430.
97. Panzer, M. J. and Frisbie, C. D. 2005 Polymer electrolyte gate dielectric reveals finite windows of high conductivity in organic thin film transistors at high charge carrier densities. *J. Am. Chem. Soc.* 127:6960–6961.
98. Xia, Y., Cho, J., Paulsen, B., Frisbie, C. D., and Renn, M. J. 2009 Correlation of on-state conductance with referenced electrochemical potential in ion gel gated polymer transistors. *Appl. Phys. Lett.* 94:013304.
99. Frisch, M. J., Trucks, G. W., Schlegel, H. B. et al. 2009 Gaussian 09 (Gaussian, Inc., Pittsburgh, PA), A.7.
100. McCreery, R. L. 2009 Electron transport and redox reactions in molecular electronic junctions. *Chem. Phys. Chem.* 10:2387–2391.
101. Yeganeh, S., Galperin, M., and Ratner, M. A. 2007 Switching in molecular transport junctions: Polarization response. *J. Am. Chem. Soc.* 129:13313–13320.
102. Tsuruoka, T., Terabe, K., Hasegawa, T. et al. 2012 Effects of moisture on the switching characteristics of oxide-based, gapless-type atomic switches. *Adv. Funct. Mater.* 22:70–77.
103. Chan, W. K., Haverkate, L. A., Borghols, W. J. H. et al. 2011 Direct view on nanoionic proton mobility. *Adv. Funct. Mater.* 21:1364–1374.
104. Waser, R. and Aono, M. 2007 Nanoionics-based resistive switching memories. *Nat. Mater.* 6:833–840.